1 # Effect of bending-torsion on fracture and fatigue life for 18Ni300

2 # steel specimens produced by SLM

3 **Wojciech Macek[1, 2, *], Reza Masoudi Nejad[3], Shun-Peng Zhu[3, 4], Jarosław Trembacz[5], R. Branco[6], J.D. Costa[6], J.A.M.**

4 **Fereira[6], C. Capela[6]**

5 [1] Faculty of Mechanical Engineering and Ship Technology, Gdańsk University of Technology, 11/12 Gabriela Narutowicza Street, 80-233 Gdańsk, Poland;

6 wojciech.macek@pg.edu.pl

7 [2] Advanced Materials Center, Gdańsk University of Technology, ul. Narutowicza 11/12, 80-233 Gdańsk, Poland;

8 wojciech.macek@pg.edu.pl

9 [3] School of Mechanical and Electrical Engineering, University of Electronic Science and Technology of China, Chengdu, P. R. China;

10 masoudinejad@uestc.edu.cn; zspeng2007@uestc.edu.cn

11 [4] Institute of Electronic and Information Engineering of UESTC in Guangdong, Dongguan 523808, China

12 zspeng2007@uestc.edu.cn

13 [5] Opole University of Technology, Opole, Poland;

14 j.trembacz@po.edu.pl

15 [6] CEMMPRE, Department of Mechanical Engineering, University of Coimbra, 3030-788 Coimbra, Portugal

16 ricardo.branco@dem.uc.pt; jose.domingos@dem.uc.pt; martins.ferreira@dem.uc.pt; carlos.capela@ipleiria.pt

17

18 * corresponding author: wojciech.macek@pg.edu.pl

19 **Abstract:** In this study, different fracture surfaces caused by fatigue failure were generated from 18Ni300 steel produced by selective laser melting

20 (SLM). Hollow round bars with a transverse hole were tested under bending-torsion to investigate the crack initiation mechanisms and fatigue life.

21 Next, the post-failure fracture surfaces were examined by optical profilometer and scanning electron microscope. The focus is placed on the

22 relationship between the fatigue features (e.g., bending-torsion ratio, fatigue crack initiation angles, and fatigue life) and the fracture surface

23 topography parameters (e.g., height parameter Sx, volume parameters Vx, maximal pit and valley angles). The analysis was carried out using the

24 entire fracture surface of the tested specimens. It was found that the decrease of the shear stress level significantly reduces the value of the fracture

25 surface parameters. A fatigue life prediction model based on both the surface topography values and the applied load was proposed. Fatigue life

26 predictions for different loading ratios agreed well with the experimental results and were slightly better than those of other existing models. The

27 proposed model can be helpful for post-mortem analysis of engineering components subjected to multiaxial fatigue.

28 **Keywords:** multiaxial fatigue, bending-torsion, notch effect, fatigue fracture, surface topography, SLM, fatigue crack initiation, fatigue life esti-

29 mation, strain energy density.

30 **Highlights**

31 • Effect of bending-torsion loading on fracture surface topography is evaluated.

32 • The bending-torsion ratio significantly affects the fracture surface topography.

33 • Fatigue life predicted from fracture surface parameters and local von Mises stresses.

34

35 ## 1. Introduction

36 In the literature focused on fatigue design, much experimental studies about the failure mechanisms exist (Azevedo and

37 Marques, 2010; Djukic et al., 2019; Jamali et al., 2016; Walczak and Szala, 2021). In particular, fatigue research attempts to reflect

38 the actual stress state (Meischel et al., 2016; Stanzl-Tschegg, 2017; Strzelecki and Wachowski, 2022) but also attempts to understand

the mechanisms associated with pure loadings (Yao et al., 2018). To gain more insight into the failure mechanisms, the investigation of multiaxial fatigue is of high interest (Gosch et al., 2020; Jamali et al., 2019; Pejkowski and Skibicki, 2019; Tomczyk and Seweryn, 2017). Fatigue life under mixed-mode loading is very important from a safety point of view (Demir et al., 2019). This is why this problem is often analyzed in scientific works, aiming to develop new research methods and better identify the governing variables. Different types of specimen geometries for mixed-mode loading have been used in literature (Wojciech Macek et al., 2021b; Rozumek et al., 2022, 2018; Vojtek et al., 2013). Furthermore, different models have been introduced to analyse the fracture behaviour under mixed-mode loading (Branco et al., 2018, 2015; Kondo et al., 2019; Pelegatti et al., 2021; Stamoulis and Carrere, 2020).

Selective laser melting (SLM) is one laser additive manufacturing technique capable of printing metal components (Branco et al., 2021b; Li et al., 2019; Santos et al., 2016; Wang et al., 2019). This technique fabricates three-dimensional objects from laser radiation to powder materials on the powder beds through successive layer bonded to already existing layers under protective atmosphere (Santos et al., 2016). Despite some interesting advantages, e.g. the geometric freedom and reduced time-to-market, it has some shortcomings, namely internal defects and high surface roughness, which may cause stress concentration effects affecting the fatigue resistance (Branco et al., 2021a; Le et al., 2019). Malekipour et al. (2021) modelled the damage of small-scale porosities on fatigue behaviour in the high-cycle regime of SLM AISI 316 steel specimens (Malekipour et al., 2021). These authors concluded that the inherence of small-scale porosities with a length lower than 5 μm did not accelerate the damage growth, except when these defects were situated in the path of the crack growth. Thus, imperfections, which have a random nature in materials elaborated by additive manufacturing, are challenging to control both in the production process and, later, in the fatigue design stage (Cunha et al., 2022; Elkhateeb et al., 2022; Garcias et al., 2021). The anisotropy of SLM produced materials can affect the fatigue crack growth rates, depending on the relation of the crack growth direction and the grain long axis. The anisotropic behavior of SLM materials was confirmed in several studies (Avanzini, 2022; Fergani et al., 2018), where the fatigue crack propagation was related to the building orientation.

Scientists are continually attempting to find more efficient solutions for engineering problems as well as to develop new research techniques. These research techniques can be divided into non-destructive and destructive approaches (Gryguc et al., 2018; Molent et al., 2017). An example of a recent study combining both non-destructive and destructive approaches is the in-depth research of underwater welded S460N steel provided by Tomków et al. (Tomków et al., 2020). They performed non-destructive tests - comprising visual, penetrant, radiographic, and ultrasonic tests - and destructive tests, which included static tensile, bending, hardness, and impact tests. In the context of fatigue analysis, there are also novel fatigue testing methods. An interesting study is, for example, the one carried out by Brodie et al. (2022) on low-cycle-fatigue of small-scale specimens. The introduction of new

68 measurement methods, e.g. Digital Image Correlation (DIC), in the analysis of crack propagation problems is another challenging

69 area. Karen et al. (2022) studied blunt notches by using the DIC measurements (Karen Alavi et al., 2022) and demonstrated its

70 accuracy in the determination of the stress fields for different geometric discontinuities, including V-, O-, and U-notches under

71 mode-I loading.

72 Profilometry began to be applied in the 1940s, pressed for the need to improve the quality of mechanical components used

73 during the World War II. Therefore, much later than the study of fatigue and fracture phenomena, but also intensely (Buljac et al.,

74 2018). The importance of surface texture analyses can be seen, among others, by the growing number of parameters contained in

75 the ISO and ASME standards (Krolczyk et al., 2018; Przemysław Podulka, 2021; Todhunter et al., 2017a). Areal surface texture

76 was born in the 1990s by extending profile paramters to 3D. Contemporary, not only in science but especially in industry,

77 profilometers are widely used (Senin et al., 2017; Zhang et al., 2022). Technologically advanced measurement stands, including

78 focus variation microscopy (FVM), are commercially available (W. Macek et al., 2021; Newton et al., 2019). Measurement devices

79 of this type have also found application in the analysis of surface topography of fatigue fractures (Lauschmann et al., 2019; Santus

80 et al., 2022; Wietecha-Reiman et al., 2022).

81 In the scientific literature on fractography, there are many attempts to find a way to quantify fatigue fractures and make them

82 dependent on damage-generating factors (de Freitas et al., 2017; Deng et al., 2022; Merson et al., 2017; Westermann et al., 2016).

83 One of these ways is the FRASTA method, but it focuses on regions from initiation to final fracture (Kobayashi and Shockey, 2010;

84 Sampath et al., 2018). On the contrary, the method introduced by the authors is based on the entire fracture area and has been

85 successfully tested for different materials and specimens geometries (Wojciech Macek et al., 2021c, 2021a).

86 Models for estimating fatigue life allow engineers to optimise structural and mechanical design (Deng et al., 2023; Masoudi

87 Nejad et al., 2022). However, there are also attempts to use other approaches. Thermodynamics fundamental equation for high-

88 cycle metal fatigue was introduced by Lee and Basaran (Lee and Basaran, 2022). Another attempt to combine additional parameters

89 involved in the fatigue process was proposed by Fan and Zhao (Fan and Zhao, 2022) by using quantitative thermography for fatigue

90 life prediction of welded components. In this case, the energy dissipation was taken as an efficient index of fatigue damage and was

91 used to develop a nonlinear damage accumulation model.

The possibility of describing the fatigue fracture process and the fatigue durability of three-dimensional metallic parts

produced by SLM based on metrological fractographic analysis and fatigue damage parameters was the main motivation to

undertake the present study. To the best of the authors' knowledge, studies dealing with this combined approach of fractographic

and fatigue damage quantifiers under multiaxial loading for SLMed materials do not exist in the open literature. Thus, first it is

examined the influence of mixed-mode loading on fracture and fatigue behavior of 18Ni300 steel specimens produced by SLM

97 using fracture surface parameters. Then, a simple fatigue life prediction model based on post-mortem fracture surface topography

98 results and local stress obtained using the finite element method is proposed. Finally, the predicted lives are compared with the

99 experimental values and those obtained from a well-known energy-based approach.

100

2. Materials and Methods

2.1. Material and fatigue test procedure

103 The material used in this study was 18Ni300 steel produced by SLM. The nominal chemical composition and the mechanical

104 properties of the tested batch are summarised in Table 1 and Table 2, respectively (Branco et al., 2021b; Macek et al., 2020). The

105 manufacturing process comprehend the deposition of 40 μm thick layers, with a hatch spacing of 100 μm, for a scan speed of 200

106 mm/s. Based on the procedure described in the ASTM E3, and as displayed in Figure 1, the optical examination revealed a lath

107 microstructure, rather coherent, and mainly formed by elongated grains, with about 150 μm long and 30-35 μm width (see Fig 1(a)).

108 It was also observed martensitic needles across the surface (see the circle in Figure 1(b)) as well as small porosities (see the dark

109 dots in Fig. 1).

a)   b)
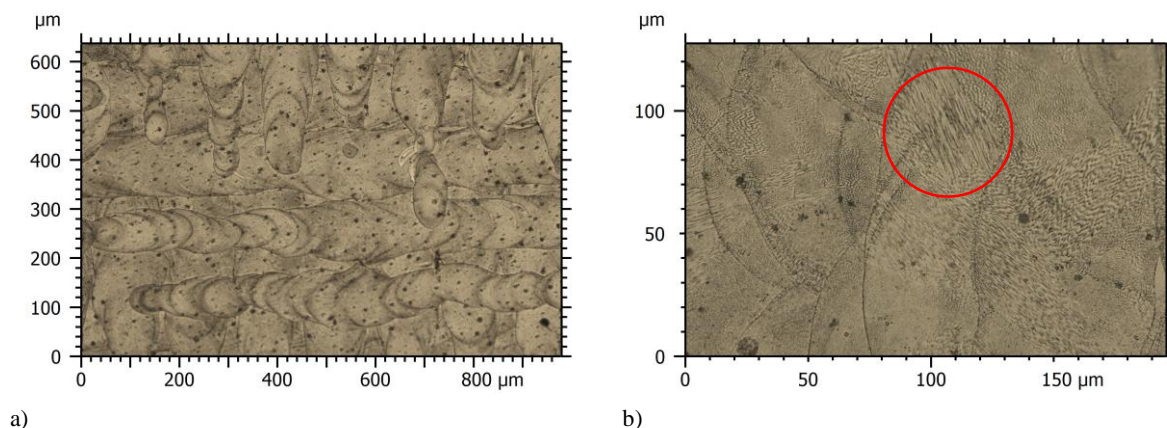
Figure 1. Microstructure of the SLM 18Ni300 examined by optical microscopy from a specimen polished and etched with picral: (a) 100×; and (b) 500× maginfication.

114

The specimens had a circular hollow geometry with an open hole in one side and were fabricated in a vertical orientation on

the base plate using a Concept Laser M3 linear printing system equipped with a Nd:YAG fibre laser. After the additive

manufacturing process, the specimens were machined and the hole region was carefully polished to a scratch-free condition by

means of progressively finer grades of silicon carbide papers (P600-grit, P1200-grit, and P2500-grit) followed by a 6-μm diamond

water-based polishing paste. Figure 2 shows the shape and dimension of the tested specimens.

4

121   **Table 1.** Nominal chemical composition of the SLM AISI 18Ni300 (wt.%) (Branco et al., 2021b; Macek et al., 2020).

C	Ni	Mn	Co	Mo	Ti	Al	Cr	P	Si	Mn	Fe
0.01	18.2	0.65	9.0	5.0	0.6	0.05	0.3	0.01	0.1	0.04	Balance

122

123   **Table 2.** Mechanical properties of the SLM AISI 18Ni300 for the tested batch (Branco et al., 2021b; Macek et al., 2020).

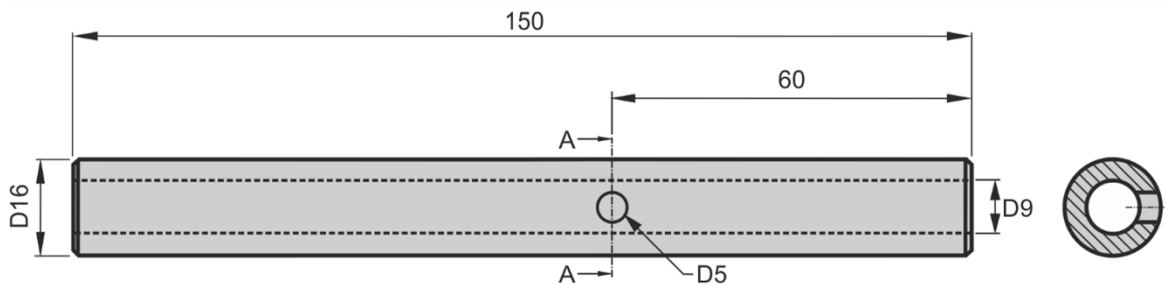| Property	Value
Porosity, ϕ (%)	0.74
Density, ρ (g/cm^3)	7.42
Poisson's ratio, υ (-)	0.33
Young's modulus, E (GPa)	168
Tensile strength, σ_{UTS} (MPa)	1147
Yield strength, σ_{YS} (MPa)	910
Strain at failure, ε_t (%)	5.12
Cyclic hardening coefficient, k' (MPa)	1921.21

124

125

126   **Figure 2.** Specimen geometry used in the multiaxial fatigue tests (units: millimetres).

127

128   The tests were performed in air, at room temperature, using sinusoidal waves, and cyclic frequencies in the range 3–6 Hz. The

129 bending moment to torsion moment ratios, *B/T*, also presented in Table 3, were equal to 1, 2 and 2/3. For all tested specimens, the

130 stress ratio, *R*, was equal to 0. The nominal normal stress amplitude σ_a and shear stress amplitude τ_a applied in the test are also listed

131 in Table 3. Crack detection and crack growth were monitored in situ via a high-resolution digital camera. In this study, the fatigue

132 life associated to crack initiation, N_i, was calculated from the experimental *a-N* curves (i.e. crack length versus number of cycles)

133 for a fixed crack length of 0.5 mm. Regarding the total life, N_f, it was estimated also from the experimental *a-N* curves for a crack

134 length of 3 mm.

Table 3. Summary of the multiaxial fatigue testing program.

Specimen	*B/T ratio*	σ_a/τ_a	σ_a (MPa)	σ_m (MPa)
BT3_2	2/3	4/3	55.27	60.79
BT3_1	2/3	4/3	79.59	87.55
BT1_1	1	2	66.32	72.96
BT1_2	1	2	79.59	87.55
BT1_3	1	2	95.50	105.05

5

|				
BT2_1	2	4	78.26	86.09
BT2_2	2	4	79.59	87.55
BT2_3	2	4	95.50	105.06

σ_a: nominal normal stress amplitude; σ_m: nominal normal mean stress; τ_a: nominal shear stress amplitude; τ_m: nominal shear mean stress

2.2. Fracture surface measurement

A Focus Variation (FV) method, applied in an Alicona profilometer (Alicona Imaging GmbH, Graz, Austria) shown in Figure 3, was used to determine the fracture surface parameters (Macek, 2021a; Macek, 2021c). This non-contact measuring system uses a white light source to project light beams onto a specimen's surface. The reflected light rays appear from the measured surface and are processed by means of a precise sensor.
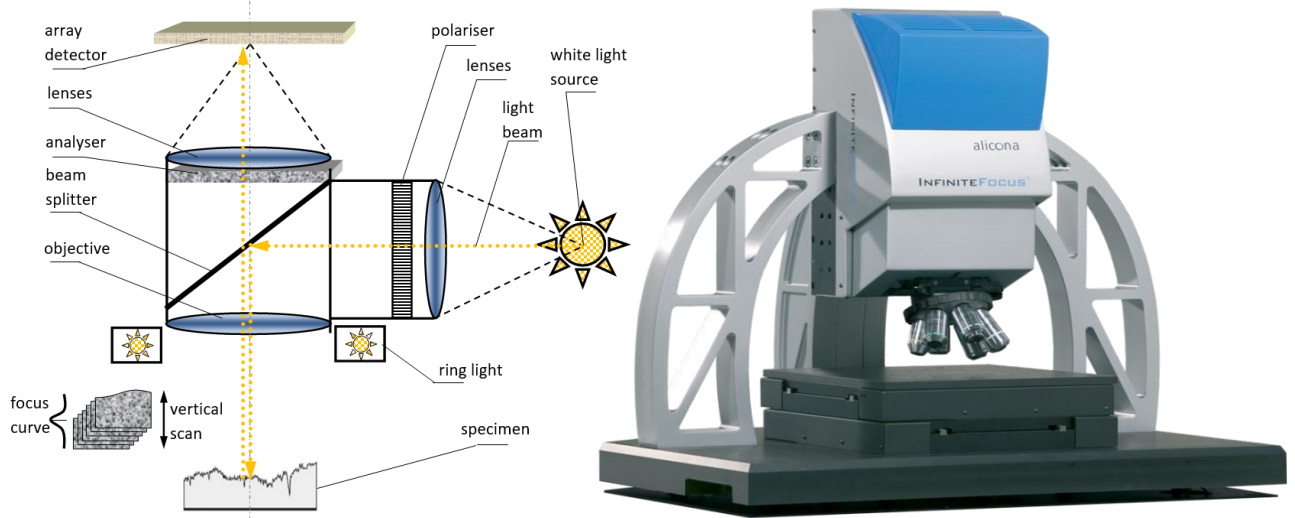
Figure 3. Alicona IF G4 profilometer used in the fracture surface measurements: (a) operation scheme; (b) picture without accessories.

The FV method combines the small depth of focus of an optical system with a vertical scanning to provide topographical information from the focus variation. The measurement device was equipped with a motorized nosepiece using five dedicated microscopic objective lenses with magnifications varying from 2.5× to 100×. For the analysis of the 18Ni300 steel specimens produced by SLM, 10× objective lenses for the entire fracture surface areas, and 100× for local fracture zones, were used. Large areas of the entire fractures were scanned using the "Image field" function across the surface, as shown in Table 4, for a 10× magnification considering 18 rows × 13 columns. Appropriately, also using the "Image field" function local fracture zones were scanned with a 100× magnification considering 13 rows × 12 columns. Stitching allowed the measurement of an area of about 14.7 mm × 15.4 mm for entire fractures. Regarding the vertical measurement range, depending on the skewness of the crack, the maximum z for the specimen with the most oblique fracture (BT3-2) was equal to 10.6 mm, and minimum z range for the specimen with $B/T = 2$ (BT2-2) was equal to 5.6 mm. The measurement parameters used during the study are listed in Table 4.

Table 4. Alicona G4 measurement device main parameters.

Parameter	Value	
Magnification	10×	100×
Vertical resolution	57.3 nm	4.7 nm
Lateral resolution	3.91 µm	1.46 µm
Number of images	19 rows × 13 columns	13 rows × 12 columns
Exposure time	138.5 µs	300.0 µs
Contrast	0.46	0.50

Surface studies were carried out on the fracture area using both height parameters, *Sx*, and volume parameters, *Vx*, according to ISO 25178 standard. The height parameters *Sx* taken into account were: *Sq, Sp, Sv, Sz*, and *Sa*. Concerning the functional parameters *Vx*, the ones considered were: *Vm, Vv, Vmp, Vmc,* and *Vvv* (Bartoszuk, 2021; P Podulka, 2021; Todhunter et al., 2017b). MountainsMap surface topography software was used to analyse and visualize the fractures (Macek, 2021b). The surface characterization also included a Texture Isotropy study which aimed to calculate the isotropy parameters with respect to a user-defined threshold, assumed here equal to 0.20. This values allowed to quantify the central zones corresponding to the portion of the peaks that remained after thresholding. The threshold equal to 0.2 is a default value but that for some metrological cases it can be right to choose an another value, in particular to provide that the central lobes are well defined and does not be in contact with the edges of the zones.

The procedure to extract the areas, called here region of interest (ROI), is summarised in Fig. 4. It can be divided into three main tasks: (1) extract the circular inside area with a radius of 4.7 mm; (2) extract the circular outside area with a radius of 7.7 mm; (3) extract the rectangular outside area of the lateral hole with dimensions of 5 mm × 5 mm. The whole surface was reduced to eliminate the regions associated with the geometric discontinuities and to obtain a uniform dimension for all samples. The lowest (Min) and highest (Max) points of the Z axis were identified for each fracture surface as well as their angles with respect to the XY plane.
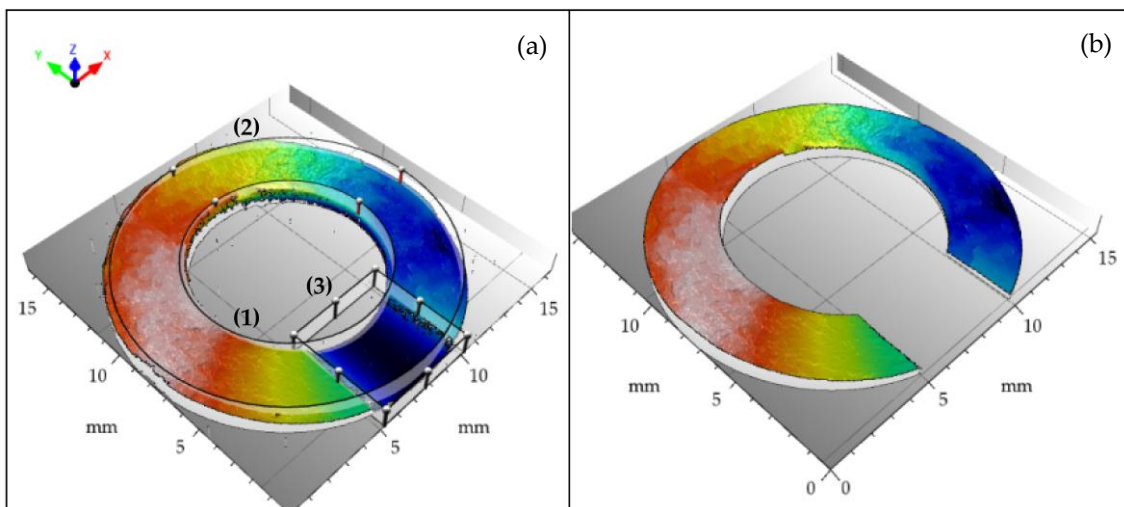

Figure 4. Scheme for determining the extracted area (BT1_2): (a) original surface; (b) region of interest.

2.3. Finite element model

The finite element model used in this study to obtain the stress field around the hole for the different *B/T* ratios is shown in Figure 5. It was created using with 4-node tetrahedral elements in an unstructured framework and contained 642,821 elements and 906,676 nodes. Around the hole, the mesh was much denser, also in the through-the-thickness direction, to better describe the stress-strain gradients acting in this region (see Fig. 5(b) and Fig. 5(c). The simulations were conducted assuming a homogeneous, linear-elastic, and isotropic material. The loading scenarios were defined by applying a single force, *F*, in the z-axis direction in the end of the rectangular cross-section arm, while the other end of the model was fixed for an extension of 30 mm from the dashed line to the right-hand side of the specimen (see Fig. 1(a)). The values of the *B/T* ratios were adjusted by changing the *L/h* ratio (*h* was fixed while *L* was determined in a case-by-case basis in order to achieve the tested values) and the magnitude of the applied load. The relationship between the nominal normal stress amplitude σ_a and the nominal shear stress amplitude τ_a can be obtained from the following formula:

$$\frac{\sigma_a}{\tau_a} = \frac{\dfrac{32\,F_a\,L}{(d_e^3 - d_i^3)}}{\dfrac{16\,F_a\,h}{(d_e^3 - d_i^3)}} \Leftrightarrow \frac{\sigma_a}{\tau_a} = \frac{2L}{h} \tag{1}$$

where d_e is the outer diameter, d_i is the inner diameter, and F_a is the force amplitude.
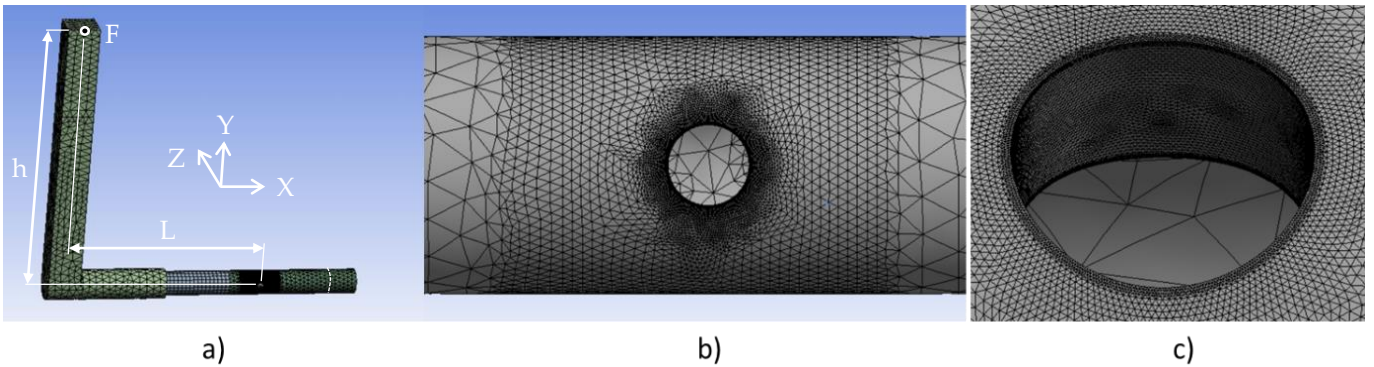
Figure 5. Finite element model of tested specimen made of SLM AISI 18Ni300 steel: (a) assembled model; (b) detail of the hole region; (c) detail of the mesh topology in the vicinity of the hole.

3. Results

3.1. Crack and multiaxial fatigue test

The different combinations of shear and normal stresses applied in the bending-torsion fatigue tests have a strong influence on crack growth direction. Depending on the mixed mode relation, as can be seen in Figure 6, various crack paths can be observed. In these geometries, the fatigue crack initiation process was characterised by the nucleation of two cracks at the hole surface in diametrically opposite locations. A similar cracking behaviour under multiaxial cyclic loading, particularly in the early stage of growth, was seen by other researchers (Gryguć et al., 2019, 2020). The crack angles at the early stage of growth, α, as expected, were also affected by the *B/T* ratio, as exhibited in Figure 6 and in Table 5. The crack angle measured on the left side was named α_1, while the crack angle measured on the right side was named α_2. As can be seen, the increase in the *B/T* ratio, i.e. the decrease of shear stress level, leads to smaller α angles. Overall, although there are some exceptions, it was also found that both α angles of the same specimen were relatively similar.
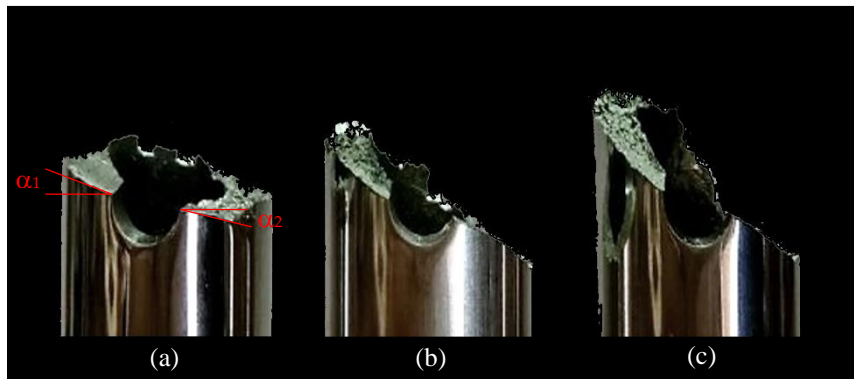
8

Figure 6. Fatigue crack initiation sites: (a) *B/T*=2; (b) *B/T*=1; and (c) *B/T*=2/3 (α_1 and α_2 represent the crack angles at the early stage of growth of the left side and the right side, respectively).

Table 5. Measured crack angles measured for the different tests in both sides of the hole.

Specimen	α_1 (degrees)	α_2 (degrees)	
BT3_2	21.92	25.26	235
BT3_1	26.16	24.86	236
BT1_1	23.2	20.25	237
BT1_2	11.98	17.01	238
BT1_3	13.98	17.45	239
BT2_1	12.15	12.62	240
BT2_2	13.56	14.11	241
BT2_3	8.13	17.59	242
α_1: angle of the first crack (left side); α_2: angle of the second crack (right side)			243

The *a-N* curves obtained in the experiments for both sides of the hole are shown in Figure 7. The measurements were fitted using third order polynomial functions, also plotted in the figure. The conventional boundaries of the curves defined to calculate N_i and N_f are marked on the graphs with bold black lines. The fatigue lives used in the analysis (both N_i and N_f) were those associated with the first crack detected in the hole. From the analysis of Figure 7, it can be concluded that in most cases, the second crack initiated after a considerable number of cycles relative to the initiation of the first crack. Nevertheless, in general, the second crack propagated faster than the first one and when the tests stopped the crack lengths were relatively similar.
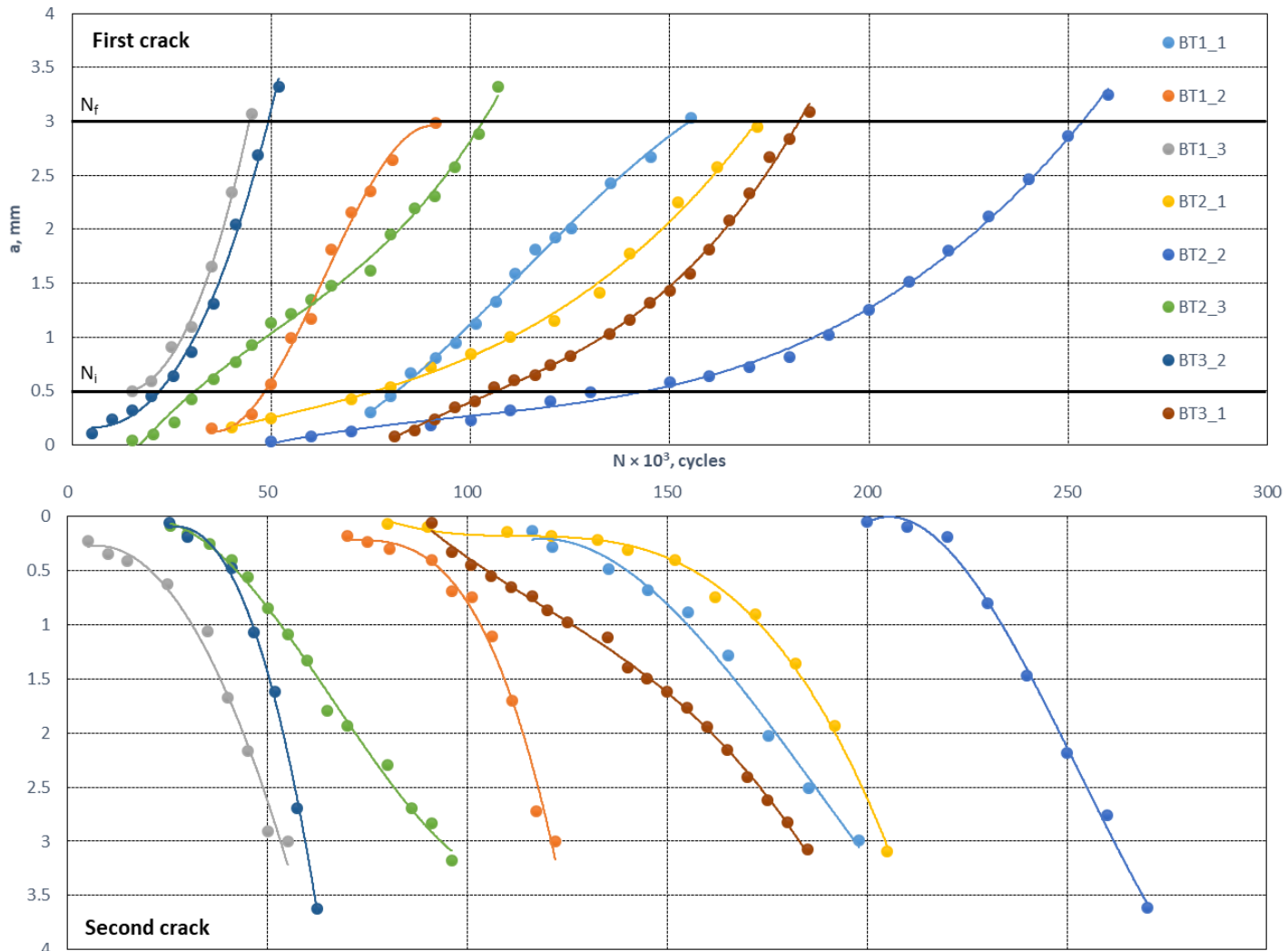
9

Figure 7. Examples of the *a/N* curves obtained from the tests for both cracks initiated in the hole region for the different *B/T* ratios.

The results of the fatigue crack initiation life N_i and the total fatigue life N_f are shown in Table 6. From Table 6, the effect of the *B/T* ratio on fatigue life is very clear. Figure 8 shows the mutual dependence between the fatigue crack initiation life and the total fatigue life for the tested cases. It is interesting to note that there is a well-defined relationship between both variables. This analysis clearly shows that the crack initiation occurs much earlier than the final fracture but, irrespective of the load conditions, the values of the N_i/N_f ratio are quite similar.
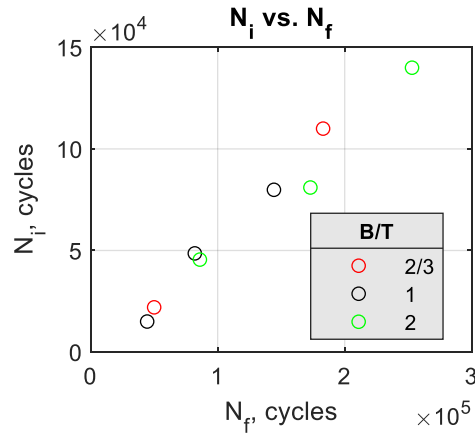
Table 6. Fatigue test results for crack initiation and total life.

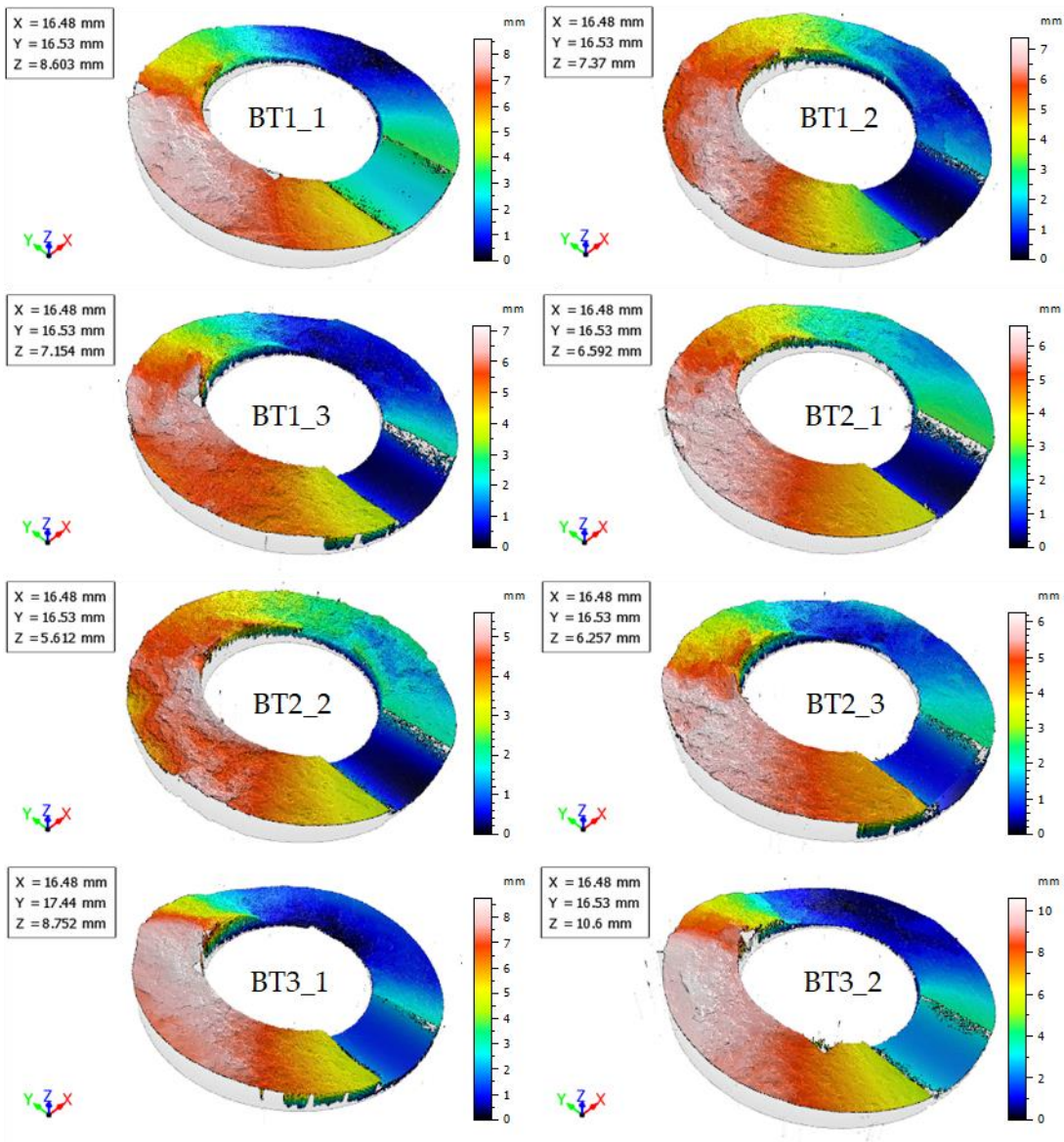| Specimen	*B/T ratio*	N_i (cycles)	N_f (cycles)
BT3_2	2/3	110,000	183,000
BT3_1	2/3	22,000	50,000
BT1_1	1	79,878	144,296
BT1_2	1	48,564	82,000
BT1_3	1	15,000	44,500
BT2_1	2	81,000	173,000
BT2_2	2	140,000	253,000

10

| BT2_3 | 2 | 45,500 | 86,000 |

Figure 8. Relationship between N_i and N_f for different *B/T* ratios.

3.2. Fracture surface topography

Figure 9 shows the fracture surfaces generated for the loading cases presented in Table 3. Figure 9(a) shows the original surfaces while Fig. 9(b) shows the ROIs. For each *B/T* ratio, without taking into account the loading level, the general patterns of the surface topography can be noted. The greater differences were noted on the z-axis scale for the cases subjected to higher shear stress levels.

11

X = 16.48 mm
Y = 16.53 mm
Z = 8.603 mm
BT1_1

X = 16.48 mm
Y = 16.53 mm
Z = 7.37 mm
BT1_2

X = 16.48 mm
Y = 16.53 mm
Z = 7.154 mm
BT1_3

X = 16.48 mm
Y = 16.53 mm
Z = 6.592 mm
BT2_1

X = 16.48 mm
Y = 16.53 mm
Z = 5.612 mm
BT2_2

X = 16.48 mm
Y = 16.53 mm
Z = 6.257 mm
BT2_3

X = 16.48 mm
Y = 17.44 mm
Z = 8.752 mm
BT3_1

X = 16.48 mm
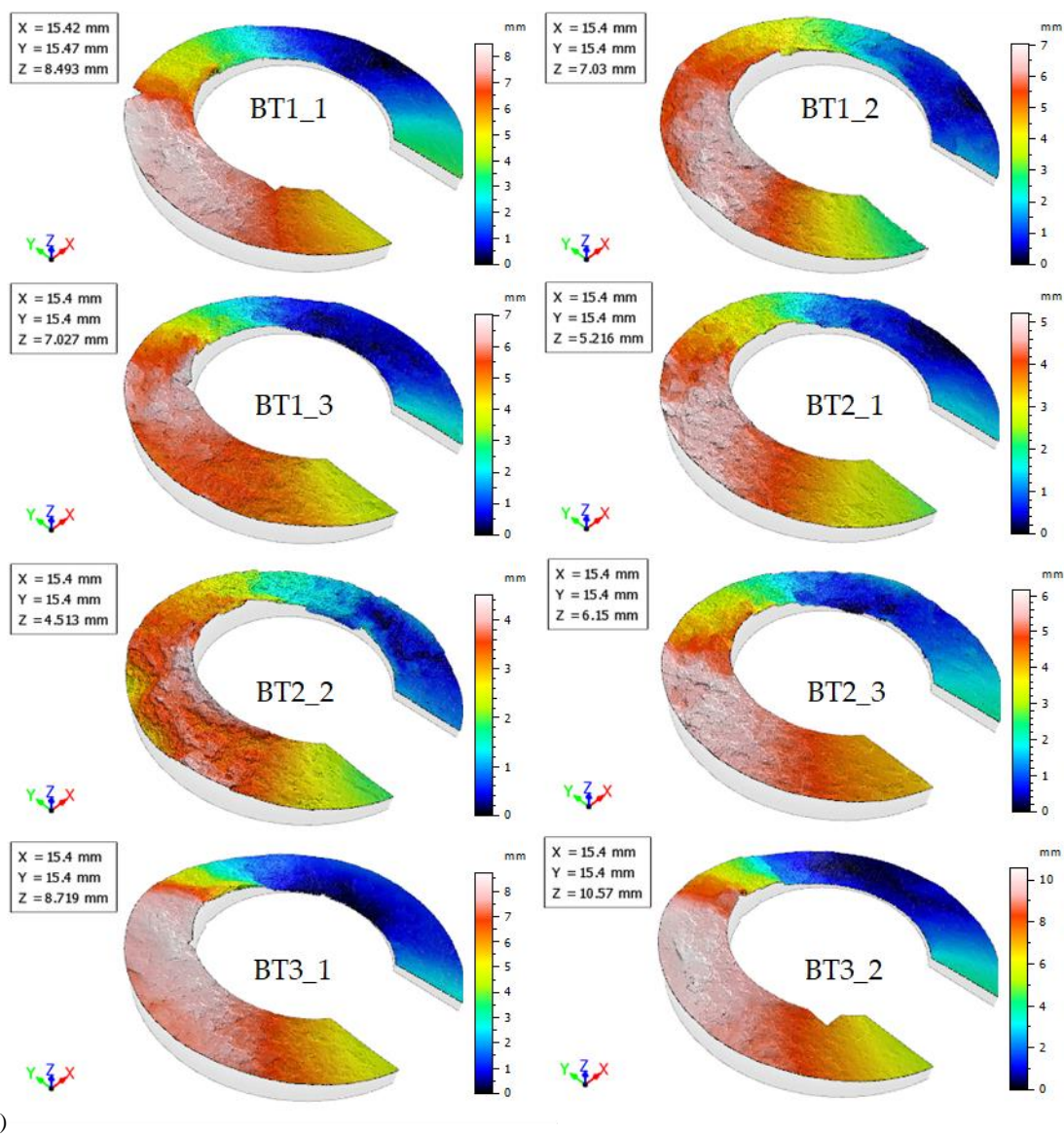Y = 16.53 mm
Z = 10.6 mm
BT3_2

(a)

12

(b)

Figure 9. Fracture surfaces acquired after the tests for *B/T*=2, *B/T*=1, *B/T*=2/3: (a) original measured surfaces; and (b) regions of interest (ROI) considered in the analysis

Table 7 summarizes the fracture surface measurements carried out for the tested geometries using both *Sx* and *Vx* parameters, respectively. The columns with the parameters of the surface topography of fatigue fractures (*Sq* and *Vv*), which were used for further analysis and presented in the discussion, are marked in green. The other parameters were also investigated but revealed to be less interesting from the perspective of developing an accurate fatigue life prediction model. Figure 10 plots all measured *Sx* and *Vx* results against the *B/T* ratios. The results show that the increase of the shear stress level, i.e. the decrease of the *B/T* ratio, leads to higher values of the fracture surface topography parameters. The loading magnitude for a fixed *B/T* ratio also has a clear effect on *Sx* and *Vx* parameters.

Table 7. Summary of the *Sx* and *Vx* results measured for the different loading cases.

Specimen	Sq	Sp	Sv	Sz	Sa	Vm	Vv	Vmc	Vvc	Vvv
	(µm)	(µm)	(µm)	(µm)	(µm)	(µm³/µm²)	(µm³/µm²)	(µm³/µm²)	(µm³/µm²)	(µm³/µm²)
BT3_2	3.71	5.46	5.10	10.57	3.45	0.024	4.764	4.289	4.695	0.069
BT3_1	3.03	4.40	4.32	8.72	2.85	0.022	3.764	3.346	3.696	0.068

BT1_1	2.68	4.40	4.09	8.49	2.41	0.020	3.750	3.010	3.650	0.100
BT1_2	2.03	3.31	3.72	7.03	1.80	0.021	2.536	2.491	2.436	0.102
BT1_3	2.15	3.79	3.23	7.03	1.99	0.030	2.720	2.510	2.670	0.050
BT2_1	1.56	2.68	2.54	5.22	1.40	0.015	2.073	1.808	2.015	0.058
BT2_2	1.22	2.25	2.26	4.51	1.10	0.020	1.450	1.440	1.390	0.060
BT2_3	1.87	3.11	3.04	6.15	1.73	0.016	2.502	2.105	2.449	0.053

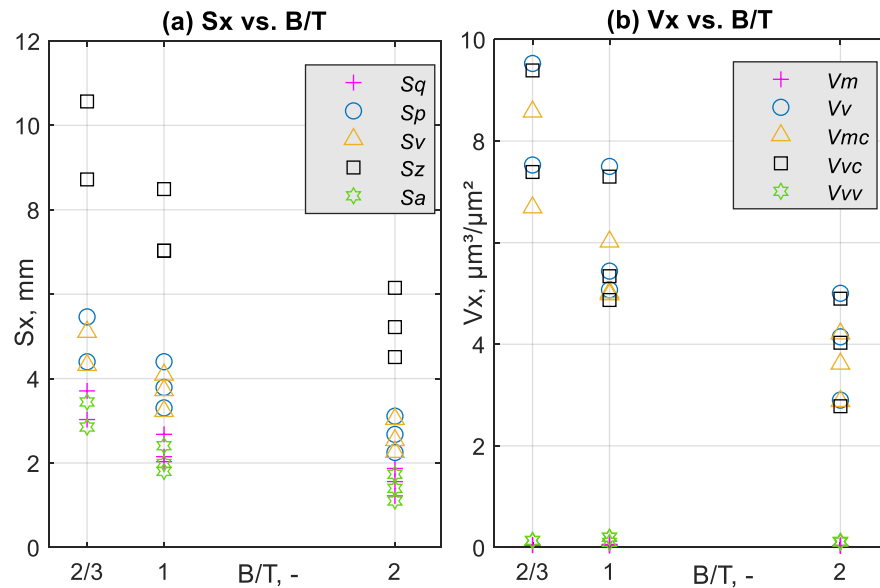Height parameters, *Sx*, and volume parameters, *Vx*, according to ISO 25178 standard.

Figure 10. Surface topography parameters versus *B/T* ratio: (a) *Sx*; and (b) *Vx*.

3.3. Maximum pit and valley locations

Figure 11 shows the location of the highest (Max) and lowest (Min) points for the extracted areas. The difference between the highest peak and the deepest valley also corresponds to the value of the *Sz* parameter, as reflected by the maximum scale value for each of the surfaces. The angles *A* and *B* associated with these two points relative to the specimen axis were also identified in the figure. It may be noticed that most of the extreme points were on the edges (inside or outside). Moreover, for the left side, the points were located in the second quadrant, while the position of the point on the right side varied between the first and the fourth quadrants.
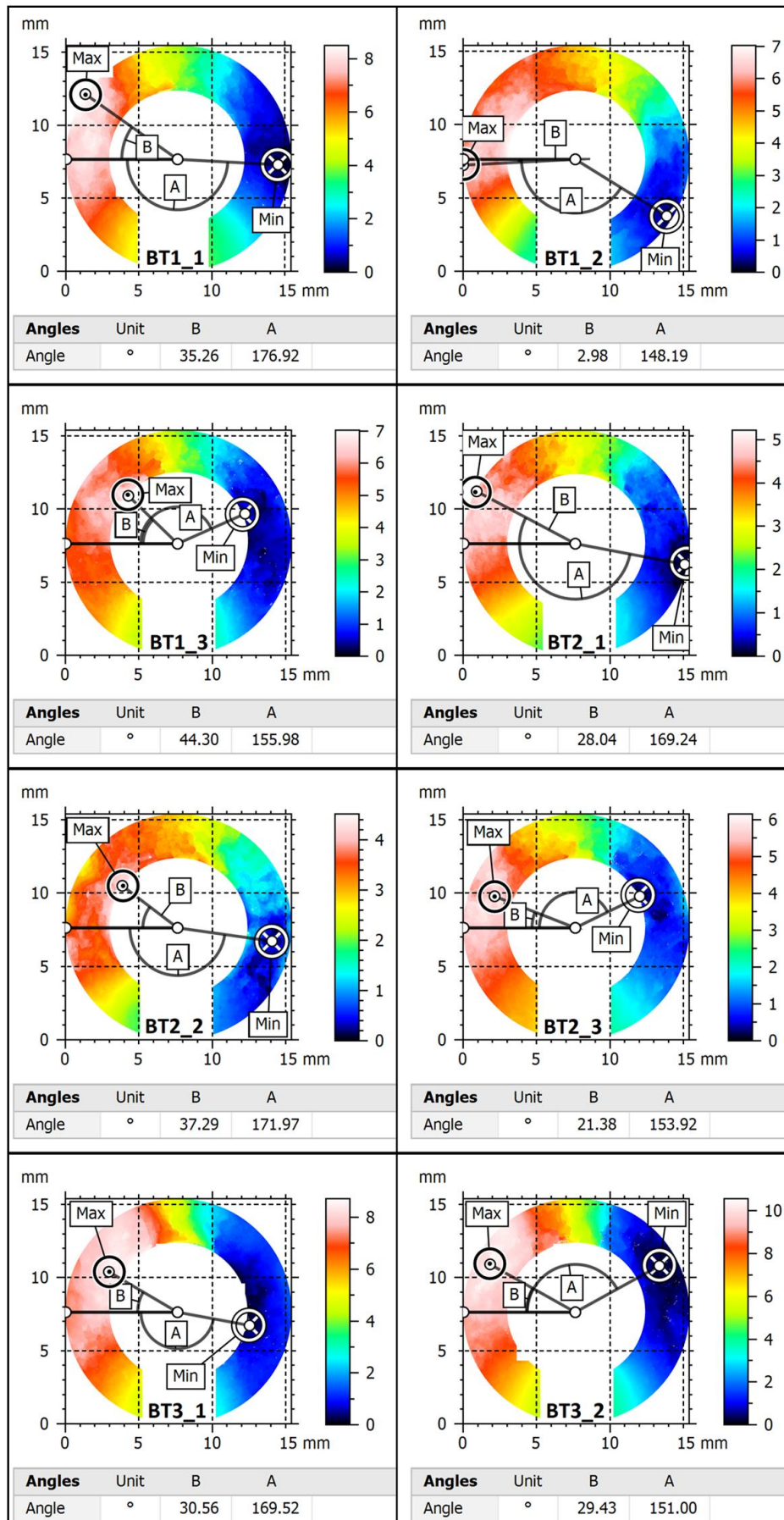
Angles	Unit	B	A
Angle	°	35.26	176.92

Angles	Unit	B	A
Angle	°	2.98	148.19

Angles	Unit	B	A
Angle	°	44.30	155.98

Angles	Unit	B	A
Angle	°	28.04	169.24

Angles	Unit	B	A
Angle	°	37.29	171.97

Angles	Unit	B	A
Angle	°	21.38	153.92

Angles	Unit	B	A
Angle	°	30.56	169.52

Angles	Unit	B	A
Angle	°	29.43	151.00

Figure 11. Maximum and minimum height of the extracted areas with their angles *A* and *B* for the different loading cases.

15

298 **Table 8.** Maximum and minimum height angles measured for the different loading cases.

299

Specimen	*A* angle (degrees)	*B* angle (degrees)
BT3_2	209.0	29.4
BT3_1	169.5	30.6
BT1_1	177.0	35.3
BT1_2	148.2	3.0
BT1_3	204.0	44.3
BT2_1	169.2	28.0
BT2_2	172.0	37.3
BT2_3	206.0	23.9

A: angle between the highest (Max) point and the x-axis of the extracted areas; *B*: angle between the lowest (Min) point and the x-axis of the extracted areas.

300

301 Figure 12 presents a 2-D scatter plot of the data relating the *A* and *B* angles with the *B/T* ratios. There is a relatively high
302 agreement of the results, either for the *A* angle or the *B* angle, regardless of the *B/T* ratio. This may suggest that all specimens had a
303 similar shape distribution of the fracture features, only differing in terms of pits and valleys, as well as in terms of broadly understood
304 roughness.
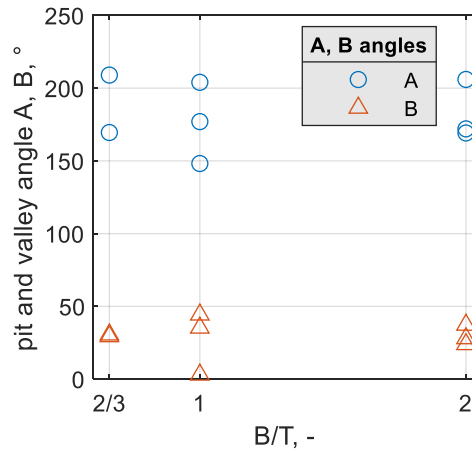
305
306 **Figure 12.** Maximum *B* and minimum *A* angles versus *B/T* ratio.

307 *3.4. Equivalent von Mises stress range*

308 The equivalent von Mises stress range $\Delta\sigma_{vM}$ used to reduce the multiaxial loading case to an equivalent unixial loading case
309 was calculated numerically, near the hole region, using the FEM models developed in this study (see Section 2.3). These values
were calculated for the node with maximum value of the first principal stress, which was assumed to be the crack initiation site. The
values obtained for the different *B/T* ratios and loading magnitudes are summarised in Table 9. Figure 13 plots $\Delta\sigma_{vM}$ against N_i (Fig.
13(a)) and against N_f (Fig. 13(b)) for the various *B/T* ratios. As can be seen, in both cases, these two variables correlate well, which
is a good intication concerning the identification of an adequate fatigue damage quantifer for this material when subjected to these
loading cases.

16

Table 9. Equivalent von Mises stress range $\Delta\sigma_{vM}$ for the different loading cases.

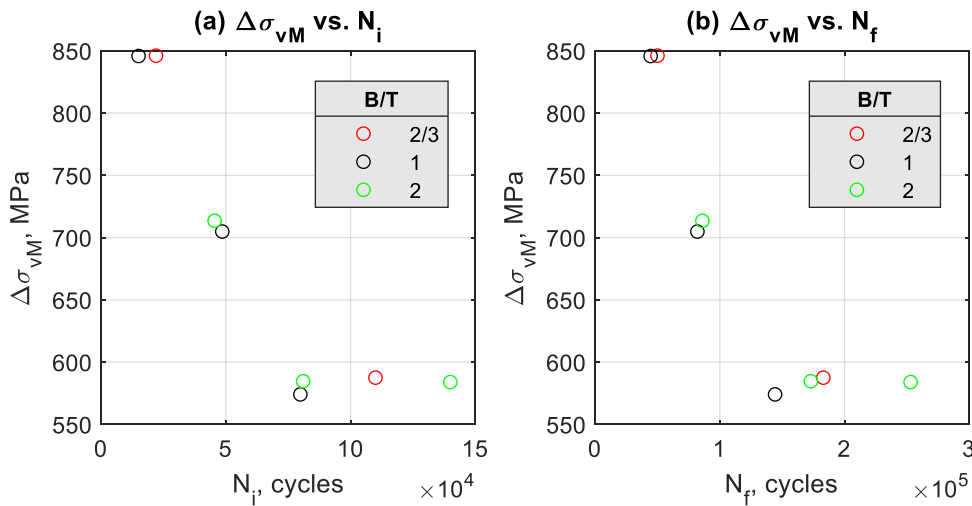| Specimen	B/T ratio	$\Delta\sigma_{vM}$ (MPa)
BT3_1	2/3	587.6
BT3_2	2/3	846.1
BT1_1	1	574.1
BT1_2	1	704.9
BT1_3	1	845.8
BT2_1	2	584.7
BT2_2	2	584.0
BT2_3	2	713.5

$\Delta\sigma_{vM}$: local von Mises equivalent stress range

Figure 13. Equivalent von Mises stress range $\Delta\sigma_{vM}$ for different *B/T* ratios versus: (a) N_i; and (b) N_f.

4. Discussion

The analysis of the tested 18Ni300 steel specimens produced by SLM based on the *B/T* ratio, crack initiation life N_i, total life N_f, crack angles α, equivalent von Mises stress σ_{VM}, maximum and minimum height of the extracted areas and the associated angles *A* and *B*, and surface parameters *Sq* and *Vv* was conducted to quantitatively identify the fracture mechanisms and an adequate fatigue damage quantifier from the post-mortem fatigued surfaces. Moreover, qualitative SEM examination and surface topography analysis of characteristic fracture areas was also taken into consideration.

4.1. Cracking mechanisms

To investigate the effects of the *B/T* ratio and both the N_i and N_f values on the fracture surface topography in terms of the total fracture area, it is important to analyse the failure mechanisms in individual fracture zones. Examples of typical defects existing in

17

337   the samples introduced during the manufacturing process are presented in Fig. 14. The three views were reconstructed from SEM
338   micrographs taken with different magnifications to illustrate the main types of defects present in the AISI 18NI300 processed by
339   SLM, namely un-melted powder particles (Fig. 14(a)); an internal void (Figure 14(b)); and a lack of fusion (Fig. 14(c)). For any
340   material, but particularly for a SLMed material, defects play a principal role in crack initiation. Characteristic defects are indicated
341   in the 3D views with red arrows. In addition, a magnified image showing un-melted powder particles is presented (see red rectangle)
342   in the upper part of Figure 14 (see the red rectangle). For the sake of clarity, common topography (z-axis) scales for the individual
343   3D views are also exhibited in the right-hand side. Voids and cavities during the cyclic loadings introduce micro stresses, possibly
344   larger than the yield stress, leading to local plastic deformation and easing the fatigue crack initiation. Obviously, if defects are
345   nearer the surface, they have a greater possibility to cause failure, since there is a smaller way for an open space.
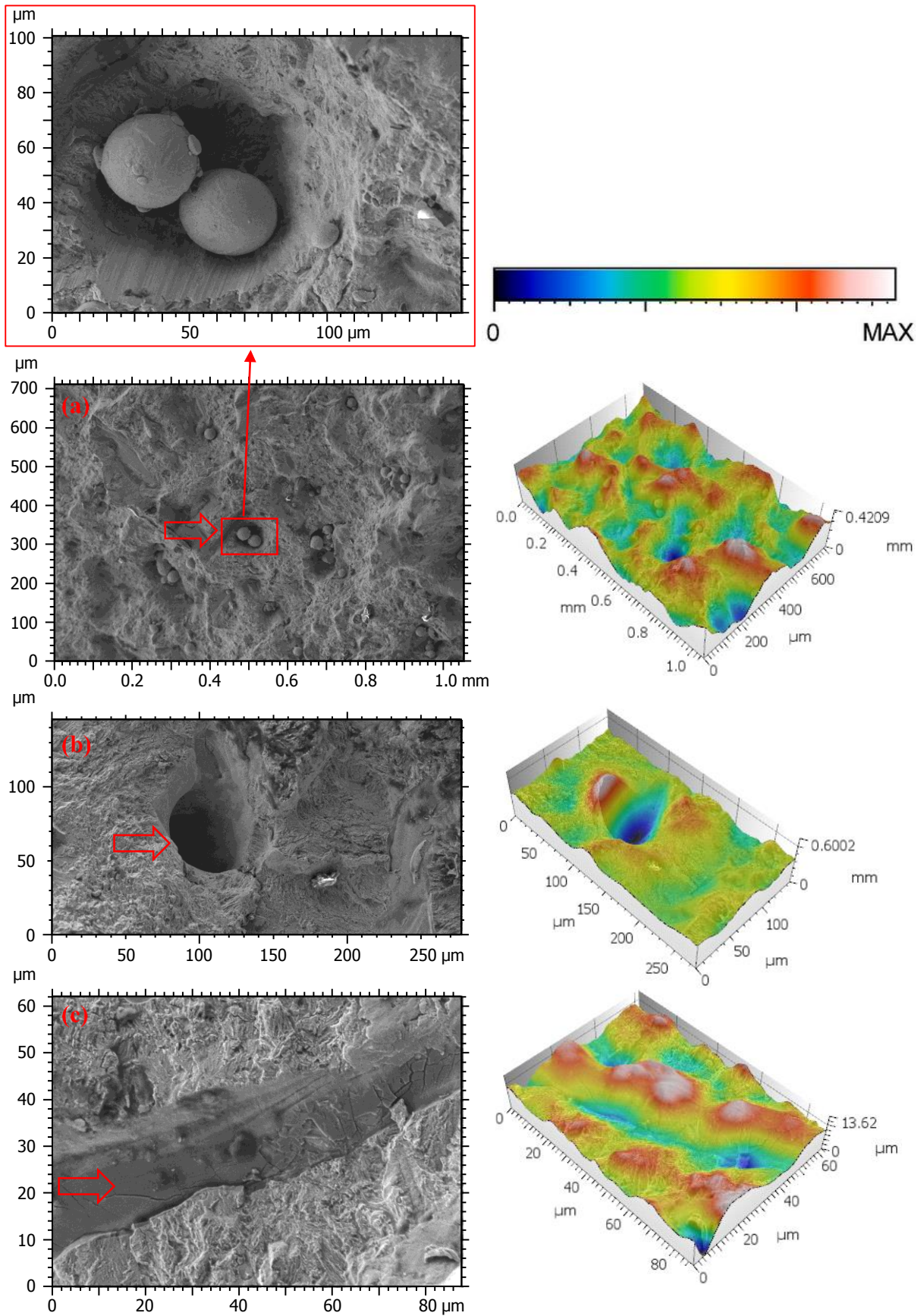
Figure 14. SEM micrograph with 3D pseudo-colour views of the reconstructed areas containing: (a) un-melted powder particles; (b) internal void; and (c) lack of fusion.

19

Surface roughness is the result of the simultaneous interaction of many independent factors, both random and determined, and as a result, it has a very complex microgeometry. There are obvious differences between individual fracture zones, as shown in Figure 15, if we compare initiation sites or propagation regions. Although these differences are obvious, the methodology proposed here considers the fractured surfaces as a total area, not distinguishing the specificities of the individual regions.

The microstructural and mechanical anisotropy, for materials produced by AM methods, occurs by itself in the process of grain formation along the build-up direction. However, the occurrence of isotropy/anisotropy on the fracture surface is rarely considered. An important property of a material or structure failure is the form of the elasto-plasticity coupled with isotropic or anisotropic damage. Nevertheless, this property is strictly related to the isotropy/anisotropy of the measured fracture surface. The directivity of the geometric structure of the surface depends on the fracture zone and it results from the kinematics of the fracture process. The isotropy of a medium is generally based on the fact that it exhibits the same physical or geometric properties in all directions. The isotropy of a surface, therefore, means that the surface has the same structure in all directions. It is also a perfectly symmetrical structure with respect to all possible axes of symmetry.

In the examined case, the isotropy was determined by analyzing the autocorrelation function (see Fig. 15). For the initiation zone, represented in the pink background of Figure 15(b), the shape of this function is asymmetric, slender, and elongated in one direction for anisotropic surfaces. The isotropy in this case was approximately 27%. On the other hand, the circular and symmetrical function graphs for isotropic surfaces reached the isotropy value of almost 83% (see Fig. 15(c), green colour).

Figure 15 also presents general information (see the top of Fig. 15) generated via MountainsMap software depending on the data supported by the AL3D file format, where information on the entire measured surface is presented on a white background (see Fig. 15(a)), and the lower part of Fig. 15 shows the distribution of slope and orientation of all triangular tiles formulating the surface with their computed values. Both histograms related to the distribution of slope and orientation of the surface have left-side concentrated distributions, especially for the initiation area. The highest value for the circular mean parameter was found for the propagation surface (26.512°) whereas the lower value (19.382°) was associated with the initiation region. The mean resultant length parameter has a value of about 0.9 for both zones. Moreover, the main parameter had the highest value for the initiation zone (11.534°) whereas for the propagation region it was equal to 5.215°.

Identification card (c)

Axis:	X		
Length:	1.450	mm	
Size:	16419	points	
Spacing:	0.088	µm	
Axis:	**Y**		
Length:	1.117	mm	
Size:	12647	points	
Spacing:	0.088	µm	
Axis:	**Z**		
Length:	792.682	µm	
Min:	154.525	µm	
Max:	947.207	µm	
Size:	792682	digits	
Spacing:	1.000	nm	
NM-points ratio:	5.180 % (1.076e+07...		

Identification card (a)

Axis:	X		
Length:	16.478	mm	
Size:	18711	points	
Spacing:	0.881	µm	
Axis:	**Y**		
Length:	16.532	mm	
Size:	18772	points	
Spacing:	0.881	µm	
Axis:	**Z**		
Length:	5.612	mm	
Min:	-0.012	mm	
Max:	5.599	mm	
Size:	5611650	digits	
Spacing:	0.001	µm	
NM-points ratio:	52.003 % (1.827e+0...		

Identification card (b)

Axis:	X		
Length:	1.449	mm	
Size:	16402	points	
Spacing:	0.088	µm	
Axis:	**Y**		
Length:	1.119	mm	
Size:	12671	points	
Spacing:	0.088	µm	
Axis:	**Z**		
Length:	463.613	µm	
Min:	16.134	µm	
Max:	479.747	µm	
Size:	463613	digits	
Spacing:	1.000	nm	
NM-points ratio:	3.783 % (7862014 P...		

(c) panel

◁ 0.200

Parameters	Value	Unit
Texture isotropy	82.774	%

Slope distribution - Fil... non-measured points

Information	
Angle	Polar angle...

Parameters	Value	...
Mode	13.500	°
Mean	27.322	°
Circular mean	26.512	°
Mean resultant length	0.927	
Main	5.215	°

(a) BT2_2 (mm)

(b) (µm)

(c) (µm)

(b) panel

◁ 0.200

Parameters	Value	Unit
Texture isotropy	27.070	%

Slope distribution - Fil... non-measured points

Information	
Angle	Polar angle...

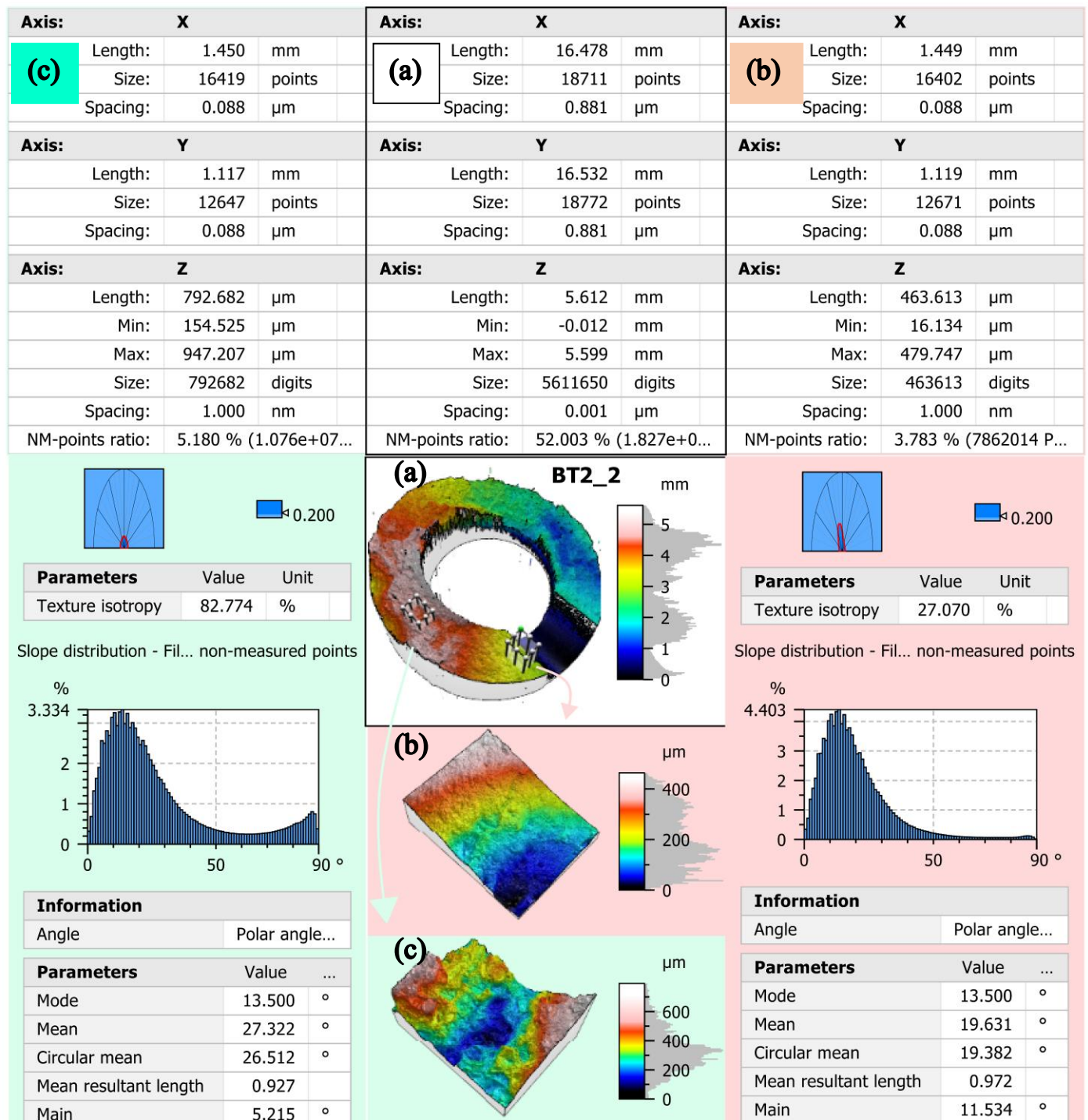| Parameters	Value	...
Mode	13.500	°
Mean	19.631	°
Circular mean	19.382	°
Mean resultant length	0.972	
Main	11.534	°

Figure 15. Identification cards for the measured data files, slope distribution histograms and (a) total fractured surface views with marked and magnified (b) initiation and (c) propagation crack zones (BT2_2 specimen).

4.2. Effect of loading conditions on fatigue crack behaviour

Fig. 16 shows four subplots regarding the relation between the: α_1 and angles α_2 (Fig. 16(a)); maximum pit A and minimum valley B (Fig. 16(b)); α angles and the equivalent von Mises stress range $\Delta\sigma_{vM}$ (Fig. 16(c)); and maximum pit and minimum valley and the equivalent von Mises stress range $\Delta\sigma_{vM}$ (Fig. 16(d)). It can be seen that both α angles increase with the shear stress component according to the sequence B/T = 2, 1, 2/3 (see Fig. 16(a)). Concerning the values of the maximum pit and minimum valley, see Fig. 16(b), the main trends are not evident. For the lower subplots, either Fig. 16(c) or Fig. 16(d)), there is no clear dependence of the analysed angles on the von Mises equivalent stress range $\Delta\sigma_{vM}$.
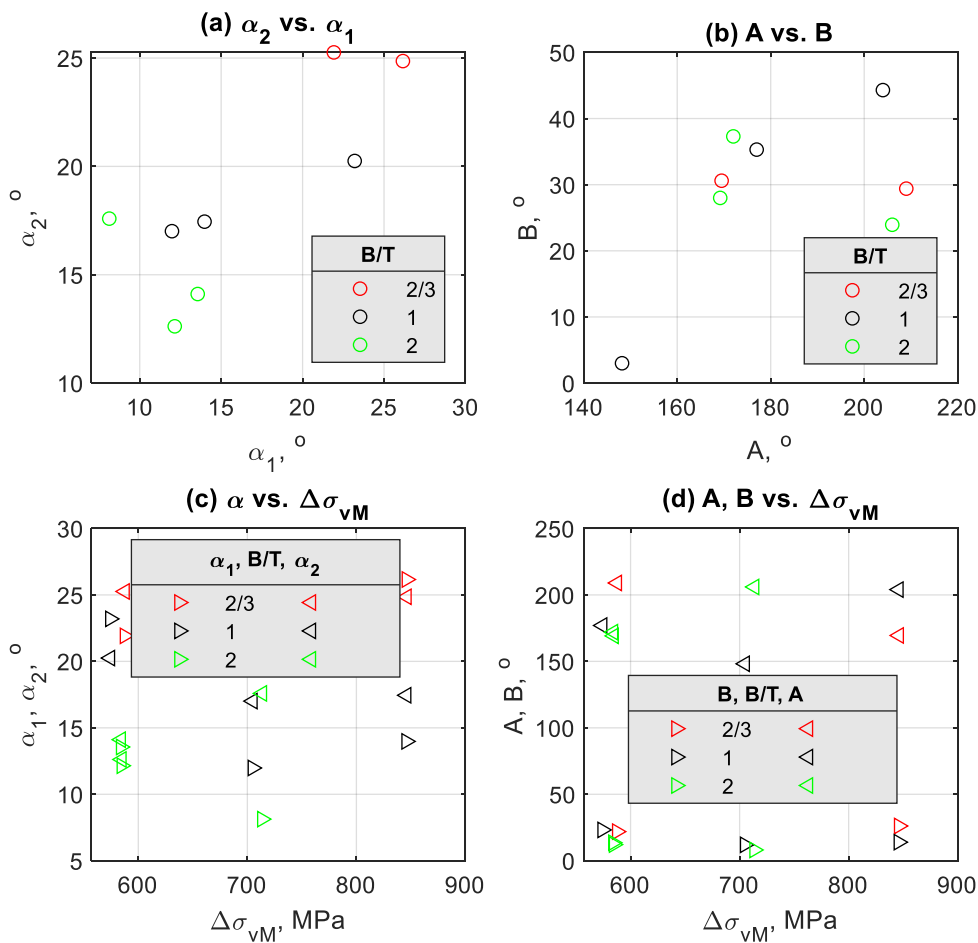
Figure 16. Relationship between: (a) α_1 and angles α_2; (b) maximum pit A and minimum valley B; (c) α angles and the equivalent von Mises stress range $\Delta\sigma_{vM}$; and (d) maximum pit A and minimum valley B and the equivalent von Mises stress range $\Delta\sigma_{vM}$.

In each boxplot of Fig. 17, the central mark (red line) indicates the median value, and the bottom and top edges of the box indicate the 25th and 75th percentiles, respectively. The whiskers extend to the most extreme data points not considered outliers, and the outliers are plotted individually using the '+' marker symbol. Based on the analysis of all specimen, according to Fig. 17(a), the median values of angles A and B, were 174.5° and 30°. the minimum values were 148.2° and 3°, and the maximum values were about 209° and 44.3°, respectively. In Fig. 17(b), for α_1 and α_2 angles, the median values were 13.77° and 17.52°, respectively. The minimum and maximum values of the crack angles were already listed in Table 5.

22
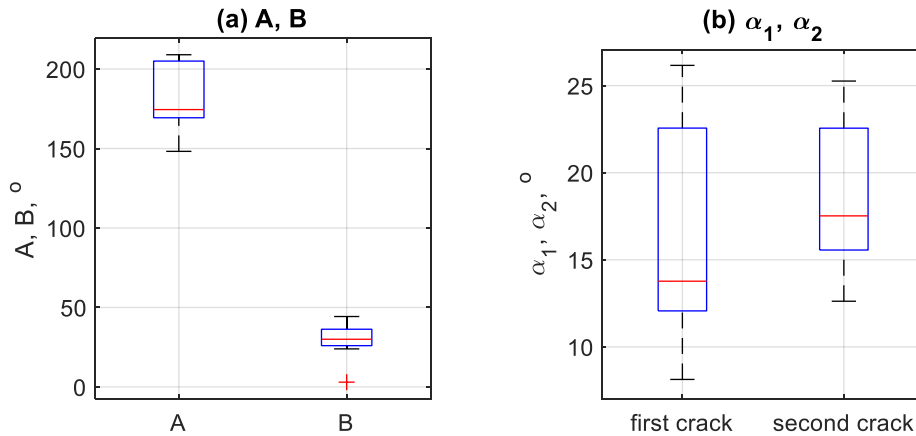
Figure 17. Boxplot: (a) maximum pit *A* and minimum valley *B*; (b) α_1 and α_2 angles.

4.3. Effect of B/T ratio, crack angles and equivalent stress range on fracture surface parameters

In order to better understand the effect of the *B/T* ratio on fracture surface features, a detailed analysis based on the *Sq* and *Vv* parameters was performed. These parameters turned out to be the most adequate based on the linear fitting analysis. Fig. 18 shows the relationship between the selected height and functional parameters (*Sq* and *Vv*) and the *B/T* ratio. The same figure shows the dependencies of the same surface topography parameters on the equivalent von Mises stress range $\Delta\sigma_{vM}$. The surface topography parameters (*Sq*, and *Vv)* decreased with increasing values of the *B/T* ratio. Fig. 19 analyses the relationship between the fracture surface parameters (*Sq* and *Vv*) and the fatigue life parameters (*N_i* and *N_f*). It is clear from these two above-mentioned figures, i.e. Fig. 18 and Fig. 19, that these parameters and the *B/T* ratio do not show satisfactory consistency in terms of linear functions for all tested specimens. Therefore, in the subsequent analysis, a combined model encompassing various parameters is used. The general tendency found from both Fig. 18 and Fig. 19 is that the smaller the *B/T* ratio, the greater the roughness.
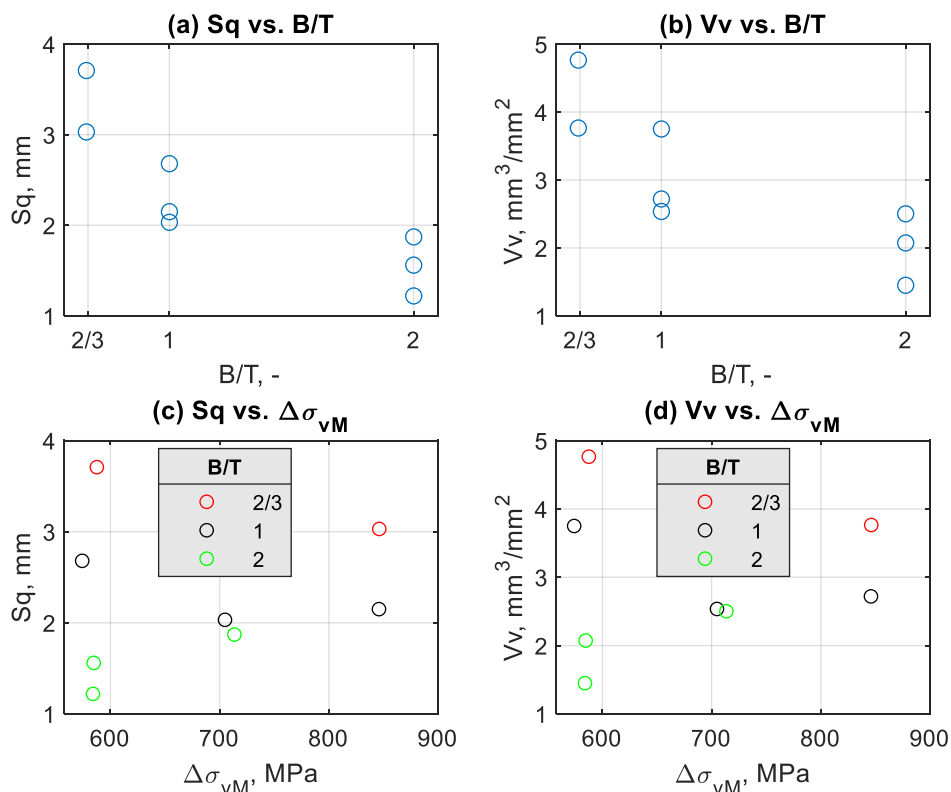
Figure 18. Relationship between the selected height *Sq* and volume *Vv* surface parameters, *B/T* ratio, and the equivalent von Mises stress range $\Delta\sigma_{vM}$; (a) *Sq* versus *B/T*; (b) *Vv* versus *B/T*; (c) *Sq* versus $\Delta\sigma_{vM}$; and (d) *Vv* versus $\Delta\sigma_{vM}$.
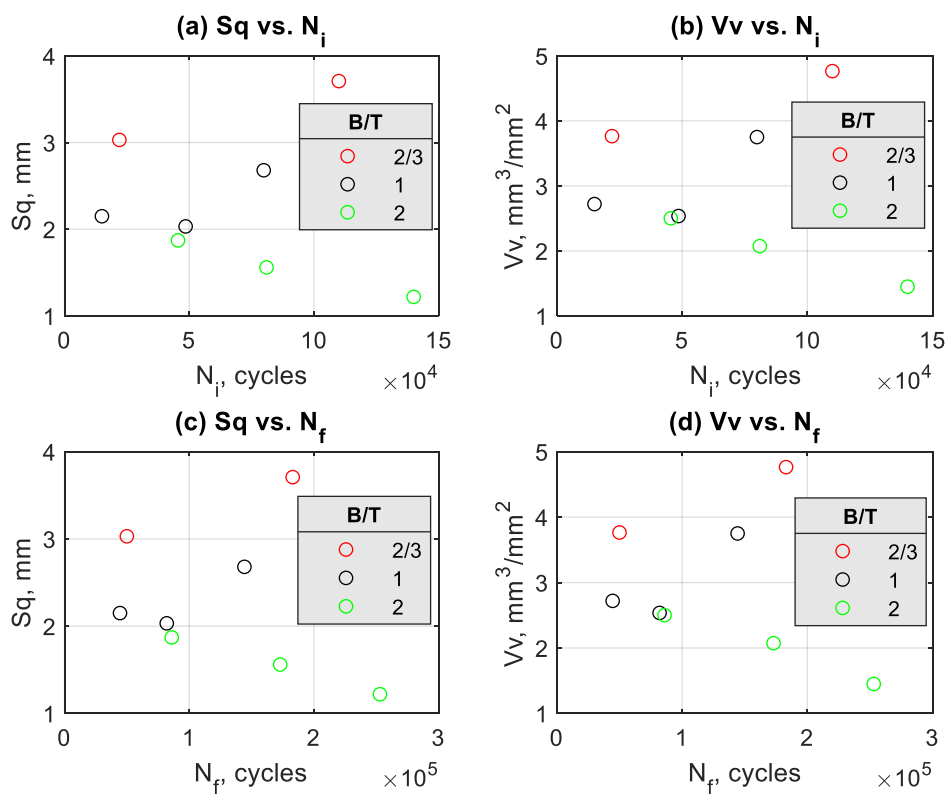

Figure 19. Relationship between the selected height *Sq* and volume *Vv* surface parameters, fatigue crack initiation life N_i, and the total fatigue life N_f; (a) *Sq* versus N_i; (b) *Vv* versus N_i; (c) *Sq* versus N_f; and (d) *Vv* versus N_f.

24

411   *4.4. Fatigue life prediction from fracture surface parameters and equivalent von Misses stress*

412   Due to the complexity of multiaxial fatigue, it is fundamental to identify robust fatigue damage parameters to effectively

413   assess the fatigue lifetime. Thus, in this study, the multiaxial fatigue life is predicted by using the novel fracture surface state

414   parameter P (see Eq. (2)) which combines two topography characteristics (the height parameter Sq, and the functional parameter

415   Vv) with the equivalent von Mises stress range, $\Delta\sigma_{vM}$. Fig. 20 plots, respectively, the equivalent von Mises stress range $\Delta\sigma_{vM}$ and

416   the P parameter against the fatigue life in terms of crack initiation life N_i (Figure 20(a) and Figure 20(b)) and total fatigue life N_f

417   (Figure 20(c) and Figure 20(d)). Through the values of the coefficient of determination R^2, it can be observed a better correlation

418   for the P parameter than for the equivalent local von Mises stress range $\Delta\sigma_{vM}$.

419

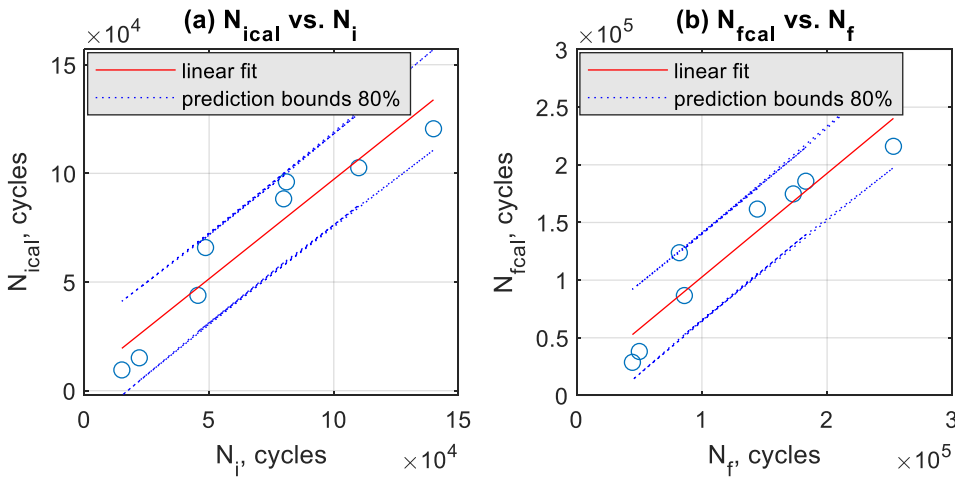420 $$P = \frac{Vv}{Sq}\Delta\sigma_{vM} \tag{2}$$

421
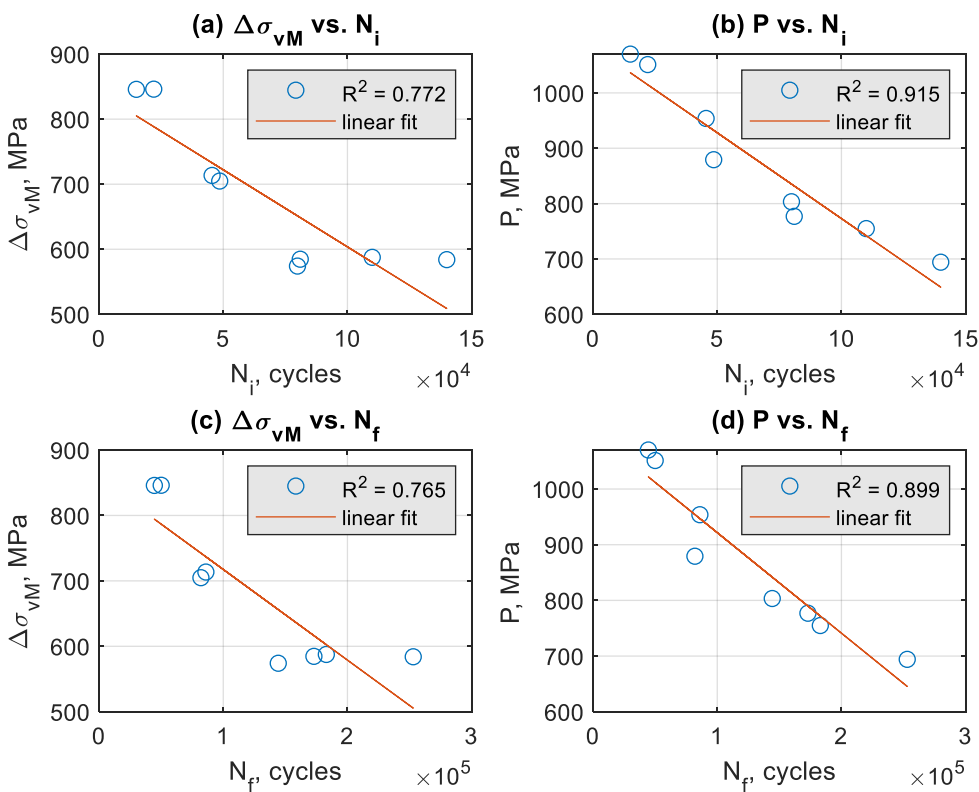
Figure 20. Equivalent local von Mises stress range $\Delta\sigma_{vM}$ and topographic stress factor P versus fatigue crack initiation life N_i and total fatigue life N_f with a linear fit: (a) $\Delta\sigma_{vM}$ versus N_i; (b) P versus N_i; (c) $\Delta\sigma_{vM}$ versus N_f; and (d) P versus N_f.

The fatigue crack initiation life N_i and the fitted fatigue crack initiation life N_{ical} computed from the fracture surface parameter function obtained from the experimental data (see Eq. (3)), i.e. a simple linear function, is compared in Fig. 21(a). The same comparison but in terms of total fatigue life N_f, carried out using the linear function defined in Eq. (4)), is presented in Fig. 21(b). As can be seen, the calculations correlate well with the experimental results for this geometry under bending-torsion loading.

25

$$N_{ical} = -295.2 \times P + 325449 \qquad (3)$$

$$N_{fcal} = -498.2 \times P + 561920 \qquad (4)$$

Figure 21. Comparison of predicted and experimental lives carried out in terms of N_i and N_f, (a) N_{ical} versus N_i; and (b) N_{ical} versus N_f.

The prediction bounds define the lower and upper values of the associated interval and define the width of the interval. The width of the interval indicates how uncertain are the fitted coefficients, the predicted observation, or the predicted fit. The bounds are defined with a level of certainty of 80%. It gives a 20% chance of being incorrect about predicting a new observation. This interval indicates 80% chance that the new fatigue test result is actually contained within the lower and upper prediction bounds. In order to better analyse the accuracy of the proposed approach, the crack initiation lives calculated with new P parameter, called here $N_{ical}(P)$, were compared to those obtained with the Smith-Watson-Topper (SWT) parameter, called here $N_{ical}(SWT)$, following the methodology introduced by Branco et al. (Branco et al., 2021a). Nevertheless, it should be noted that the Branco's approach is designed to deal with a crack length defined from the El-Haddad parameter but here, for the sake of comparability, it was applied for a crack length equal to 0.5 mm, as defined in Section 2.

Figure 22 compares the fatigue lives obtained from the two different approaches. The dashed lines correspond to a life scatter factor of 1.5, and the dotted lines correspond to a life scatter factor of 2. It can be seen that for both computational approaches, $N_{ical}(P)$ and $N_{ical}(SWT)$, there is a high agreement with the experimental values. Furthermore, the proposed model has a good agreement with the experiment data, all point fall within the ± 2 scatter bands and most of them fall within ± 1.5 scatter bands. The cases of the SWT-based approach that do not fall within the ± 1.5 scatter bands are samples with higher crack initiation life values, near 10^5 cycles, which can be seen as non-conservative exceedance. The P-based approach also has some points out of the ± 1.5 scatter bands for the minimum N_i values which can be interpreted as conservative exceedance.
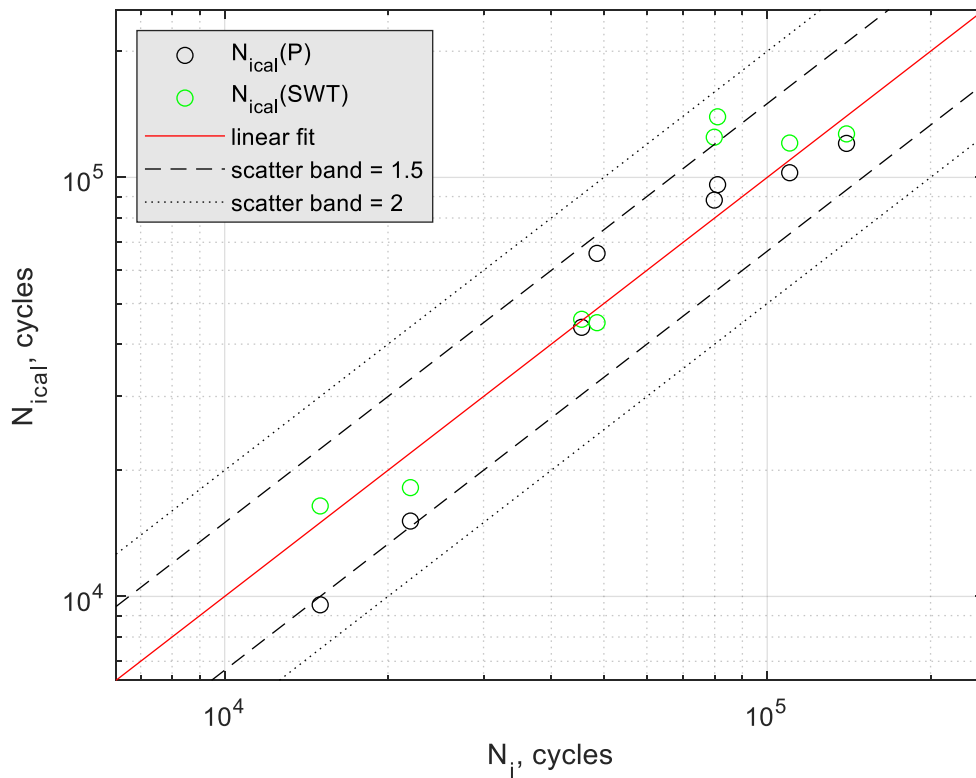
Figure 22. Comparison in log-log scales between the predicted N_{ical} and the experimental N_i.

5. Conclusions

The effect of the bending-torsion ratio *B/T* on fracture surface parameters has been studied for hollow geometries with a lateral hole made of 18Ni300 steel produced by SLM. Fatigue failure was characterised by the initiation and growth of two cracks at diametrically opposite sites around the hole surface. A quantitative analysis of the entire fracture areas of the tested specimens was performed for each loading case. A new equivalent fracture damage parameter based on the local von Misses stress range and fracture surface parameters is proposed in this study. The conclusions can be summarized as follows:

- The shear stress level had a strong influence not only on crack angles and fatigue life but also on surface topography measurements, either based on area *Sx* or volume *Vx* parameters;

- The maximum pits (Max) and the minimum valleys (Min) were located on the edges of the fracture surfaces and their distributions were similar for all specimens, irrespective of the *B/T* ratio and stress amplitude;

- For the initiation zone, the surface showed the properties of an anisotropic surface. On the contrary, for the propagation zone, the surface exhibited an isotropic property;

- The equivalent local von Mises stress range $\Delta\sigma_{vM}$ turned out to be a good fatigue damage quantifier, reason why it was used as the main component of the new *P* parameter, allowing to estimate the fatigue life;

- The model based on the SWT parameter exhibited almost similar predictive capabilities than the model based on the *P* parameter, which demonstrates the accuracy of the proposed parameter;

- The new post-failure equivalent damage parameter *P*, which accounts for the fracture surface state and the local von Mises stress range, seems to reflect the physical failure conditions of this material under bending-torsion loading;

- The fatigue lives predicted using the proposed model agreed well with the experiments, with most predictions within scatter bands with factors of ±1.5 and all points within scatter bands with factors of ±2.

Nomenclature

a	mm		crack length
A	°		Minimum point for Z axis in the XY plane angle
B	°		Maximum point for Z axis in the XY plane angle
B/T	-		bending moment to torsion moment ratio
E	GPa		Young's modulus
F	N		force
L/h	mm		finite element model dimensions ratio
N_i	cycles		number of cycles to crack initiation
N_f	cycles		number of cycles to failure
P	MPa		topographic stress factor
R	-		stress ratio
R^2	-		coefficient of determination
Sa	μm		arithmetical mean height
Sk	μm		core height
Sq	μm		root mean square height
Sz	μm		maximum height
Vmc	μm³/μm²		core material volume
Vmp	μm³/μm²		peak material volume
Vv	μm³/μm²		void volume
Vvc	μm³/μm²		core void volume
Vvv	μm³/μm²		pit void volume
k'	MPa		cyclic hardening coefficient
α	°		crack angle
ε_t	%		strain at failure
ϕ	%		porosity
ρ	g/cm³		density
σ_{YS}	MPa		yield strength
σ_{UTS}	MPa		tensile strength
υ	-		Poisson's ratio
σ_a	MPa		nominal normal stress amplitude
σ_m	MPa		nominal normal mean stress
$\Delta\sigma_{vM}$	MPa		local von Mises equivalent stress range
τ	MPa		nominal shear stress
τ_a	MPa		nominal shear stress amplitude
τ_m	MPa		nominal shear mean stress

References

Avanzini, A., 2022. Fatigue Behavior of Additively Manufactured Stainless Steel 316L. Materials 2023, Vol. 16, Page 65 16, 65. https://doi.org/10.3390/MA16010065

Azevedo, C.R.F., Marques, E.R., 2010. Three-dimensional analysis of fracture, corrosion and wear surfaces. Eng Fail Anal 17, 286–300. https://doi.org/10.1016/J.ENGFAILANAL.2009.06.010

522 Bartoszuk, M., 2021. Approximately Model of the Maximum Temperature on the Chip Surface. Materials 2021, Vol. 14, Page 2592 14, 2592.
523 https://doi.org/10.3390/MA14102592

524 Branco, R., Antunes, F.V., Costa, J.D., 2015. A review on 3D-FE adaptive remeshing techniques for crack growth modelling. Eng Fract Mech
525 141, 170–195. https://doi.org/10.1016/J.ENGFRACMECH.2015.05.023

526 Branco, R., Costa, J.D., Borrego, L.P., Berto, F., Razavi, S.M.J., Macek, W., 2021a. Comparison of different one-parameter damage laws and
527 local stress-strain approaches in multiaxial fatigue life assessment of notched components. Int J Fatigue 151, 106405.
528 https://doi.org/10.1016/J.IJFATIGUE.2021.106405

529 Branco, R., Costa, J.D., Martins Ferreira, J.A., Capela, C., Antunes, F. v., Macek, W., 2021b. Multiaxial fatigue behaviour of maraging steel
530 produced by selective laser melting. Mater Des 201, 109469. https://doi.org/10.1016/j.matdes.2021.109469

531 Branco, R., Prates, P.A., Costa, J.D., Berto, F., Kotousov, A., 2018. New methodology of fatigue life evaluation for multiaxially loaded notched
532 components based on two uniaxial strain-controlled tests. Int J Fatigue 111, 308–320. https://doi.org/10.1016/j.ijfatigue.2018.02.027

533 Brodie, E.G., Richter, J., Wegener, T., Molotnikov, A., Niendorf, T., 2022. Influence of a remelt scan strategy on the microstructure and fatigue
534 behaviour of additively manufactured biomedical Ti65Ta efficiently assessed using small scale specimens. Int J Fatigue 162, 106944.
535 https://doi.org/10.1016/J.IJFATIGUE.2022.106944

536 Buljac, A., Helfen, L., Hild, F., Morgeneyer, T.F., 2018. Effect of void arrangement on ductile damage mechanisms in nodular graphite cast iron:
537 In situ 3D measurements. Eng Fract Mech 192, 242–261. https://doi.org/10.1016/J.ENGFRACMECH.2018.01.008

538 Cunha, Â., Marques, A., Silva, M.R., Bartolomeu, F., Silva, F.S., Gasik, M., Trindade, B., Carvalho, Ó., 2022. Laser powder bed fusion of the
539 steels used in the plastic injection mould industry: a review of the influence of processing parameters on the final properties. The
540 International Journal of Advanced Manufacturing Technology 2022 121:7 121, 4255–4287. https://doi.org/10.1007/S00170-022-09588-0

541 de Freitas, M., Reis, L., Meggiolaro, M.A., de Castro, J.T.P., 2017. Stress scale factor and critical plane models under multiaxial proportional
542 loading histories. Eng Fract Mech 174, 104–116. https://doi.org/10.1016/J.ENGFRACMECH.2016.12.016

543 Demir, O., Ayhan, A.O., İriç, S., 2019. A novel test system for mixed mode-I/II/III fracture tests – Part 2: Experiments and criterion development.
544 Eng Fract Mech 220, 106671. https://doi.org/10.1016/J.ENGFRACMECH.2019.106671

545 Deng, Q.Y., Zhu, S.P., He, J.C., Li, X.K., Carpinteri, A., 2022. Multiaxial fatigue under variable amplitude loadings: review and solutions.
546 International Journal of Structural Integrity 13, 349–393. https://doi.org/10.1108/IJSI-03-2022-0025/FULL/XML

547 Deng, Q.Y., Zhu, S.P., Niu, X., Lesiuk, G., Macek, W., Wang, Q., 2023. Load path sensitivity and multiaxial fatigue life prediction of metals
548 under non-proportional loadings. Int J Fatigue 166, 107281. https://doi.org/10.1016/J.IJFATIGUE.2022.107281

549 Djukic, M.B., Bakic, G.M., Sijacki Zeravcic, V., Sedmak, A., Rajicic, B., 2019. The synergistic action and interplay of hydrogen embrittlement
550 mechanisms in steels and iron: Localized plasticity and decohesion. Eng Fract Mech 216, 106528.
551 https://doi.org/10.1016/J.ENGFRACMECH.2019.106528

552 Elkhateeb, M.G., Liu, S., Shin, Y.C., 2022. Extended mechanics of structural genome for predicting mechanical properties of additively
553 manufactured Ti6Al4V considering porosity and microstructure. Mechanics of Materials 169, 104300.
554 https://doi.org/10.1016/J.MECHMAT.2022.104300

555 Fan, J., Zhao, Y., 2022. Quantitative thermography for fatigue damage assessment and life prediction of welded components. Mechanics of
556 Materials 164, 104120. https://doi.org/10.1016/J.MECHMAT.2021.104120

557 Fergani, O., Bratli Wold, A., Berto, F., Brotan, V., Bambach, M., 2018. Study of the effect of heat treatment on fatigue crack growth behaviour of
316L stainless steel produced by selective laser melting. Fatigue Fract Eng Mater Struct 41, 1102–1119. https://doi.org/10.1111/FFE.12755

Garcias, J.F., Martins, R.F., Branco, R., Marciniak, Z., Macek, W., Pereira, C., Santos, C., 2021. Quasistatic and fatigue behavior of an AISI H13
steel obtained by additive manufacturing and conventional method. Fatigue Fract Eng Mater Struct ffe.13565.
https://doi.org/10.1111/FFE.13565

Golewski, G.L., 2022. Comparative measurements of fracture toughness combined with visual analysis of cracks propagation using the DIC
technique of concretes based on cement matrix with a highly diversified composition. Theoretical and Applied Fracture Mechanics 121,
103553. https://doi.org/10.1016/J.TAFMEC.2022.103553

565 Gosch, A., Berer, M., Hutař, P., Slávik, O., Vojtek, T., Arbeiter, F.J., Pinter, G., 2020. Mixed Mode I/III fatigue fracture characterization of
566   Polyoxymethylene. Int J Fatigue 130, 105269. https://doi.org/10.1016/J.IJFATIGUE.2019.105269

567 Gryguć, A., Behravesh, S.B., Shaha, S.K., Jahed, H., Wells, M., Williams, B., Su, X., 2018. Low-cycle fatigue characterization and texture induced
568   ratcheting behaviour of forged AZ80 Mg alloys. Int J Fatigue 116, 429–438. https://doi.org/10.1016/J.IJFATIGUE.2018.06.028

569 Gryguć, A., Behravesh, S.B., Shaha, S.K., Jahed, H., Wells, M., Williams, B., Su, X., 2019. Multiaxial cyclic behaviour of extruded and forged
570   AZ80 Mg alloy. Int J Fatigue 127, 324–337. https://doi.org/10.1016/J.IJFATIGUE.2019.06.015

571 Gryguć, A., Behravesh, S.B., Jahed, H., Wells, M., Williams, B., Su, X., 2020. Multiaxial Fatigue and Cracking Orientation of Forged AZ80
572   Magnesium Alloy. Procedia Structural Integrity 25, 486–495. https://doi.org/10.1016/J.PROSTR.2020.04.055

573 Jamali, J., Mahmoodi, M.J., Hassanzadeh-Aghdam, M.K., Wood, J.T., 2019. A mechanistic criterion for the mixed-mode fracture of unidirectional
574   polymer matrix composites. Compos B Eng 176, 107316. https://doi.org/10.1016/J.COMPOSITESB.2019.107316

575 Jamali, J., Mourad, A.-H.I., Fan, Y., Wood, J.T., 2016. Through-thickness fracture behavior of unidirectional glass fibers/epoxy composites under
576   various in-plane loading using the CTS test. Eng Fract Mech 156, 83–95. https://doi.org/10.1016/J.ENGFRACMECH.2016.01.016

577 Karen Alavi, S., Ayatollahi, M.R., Jamali, J., Petru, M., 2022. On the applicability of digital image correlation method in extracting the higher
578   order terms in stress field around blunt notches. Theoretical and Applied Fracture Mechanics 121, 103436.
579   https://doi.org/10.1016/J.TAFMEC.2022.103436

580 Kobayashi, T., Shockey, D.A., 2010. Fracture surface topography analysis (FRASTA)—Development, accomplishments, and future applications.
581   Eng Fract Mech 77, 2370–2384. https://doi.org/10.1016/J.ENGFRACMECH.2010.05.016

582 Kondo, T., Miki, D., Hirakata, H., Minoshima, K., 2019. Effects of surface oxide layer on fracture toughness of submicrometer-thick freestanding
583   copper films. Eng Fract Mech 220, 106652. https://doi.org/10.1016/J.ENGFRACMECH.2019.106652

584 Krolczyk, G.M., Maruda, R.W., Krolczyk, J.B., Nieslony, P., Wojciechowski, S., Legutko, S., 2018. Parametric and nonparametric description of
585   the surface topography in the dry and MQCL cutting conditions. Measurement (Lond) 121, 225–239.
586   https://doi.org/10.1016/j.measurement.2018.02.052

587 Lauschmann, H., Tesař, K., Jiroušková, K., 2019. Quantitative fractography of fatigue cracks: a new solution in 3D. Procedia Structural Integrity
588   23, 107–112. https://doi.org/10.1016/J.PROSTR.2020.01.071

589 Lee, H.W., Basaran, C., 2022. Predicting high cycle fatigue life with unified mechanics theory. Mechanics of Materials 164, 104116.
590   https://doi.org/10.1016/J.MECHMAT.2021.104116

591 Le, V.-D., Pessard, E., Morel, F., Edy, F., 2019. Interpretation of the fatigue anisotropy of additively manufactured TA6V alloys via a fracture
592   mechanics approach. Eng Fract Mech 214, 410–426. https://doi.org/10.1016/J.ENGFRACMECH.2019.03.048

593 Li, J., Wang, X., Qi, W., Tian, J., Gong, S., 2019. Laser nanocomposites-reinforcing/manufacturing of SLM 18Ni300 alloy under aging treatment.
594   Mater Charact 153, 69–78. https://doi.org/10.1016/J.MATCHAR.2019.04.038

595 Macek, W., 2021a. Fracture Areas Quantitative Investigating of Bending-Torsion Fatigued Low-Alloy High-Strength Steel. Metals 2021, Vol. 11,
596   Page 1620 11, 1620. https://doi.org/10.3390/MET11101620

597 Macek, W., 2021b. Fracture surface formation of notched 2017A-T4 aluminium alloy under bending fatigue. International Journal of Fracture
598   2021 1–17. https://doi.org/10.1007/S10704-021-00579-Y

599 Macek, Wojciech, Branco, R., Costa, J.D., Pereira, C., 2021a. Strain sequence effect on fatigue life and fracture surface topography of 7075-T651
600   aluminium alloy. Mechanics of Materials 160, 103972. https://doi.org/10.1016/j.mechmat.2021.103972

Macek, Wojciech, Branco, R., Costa, J.D., Trembacz, J., 2021b. Fracture Surface Behavior of 34CrNiMo6 High-Strength Steel Bars with Blind
   Holes under Bending-Torsion Fatigue. Materials 2022, Vol. 15, Page 80 15, 80. https://doi.org/10.3390/MA15010080

Macek, Wojciech, Branco, R., Korpyś, M., Łagoda, T., 2021c. Fractal dimension for bending–torsion fatigue fracture characterisation.
   Measurement 184, 109910. https://doi.org/10.1016/J.MEASUREMENT.2021.109910

Macek, W., Branco, R., Trembacz, J., Costa, J.D., Ferreira, J.A.M., Capela, C., 2020. Effect of multiaxial bending-torsion loading on fracture
   surface parameters in high-strength steels processed by conventional and additive manufacturing. Eng Fail Anal 118.
   https://doi.org/10.1016/j.engfailanal.2020.104784

608 Macek, W., 2021c. Correlation between Fractal Dimension and Areal Surface Parameters for Fracture Analysis after Bending-Torsion Fatigue.
609   Metals 2021, Vol. 11, Page 1790 11, 1790. https://doi.org/10.3390/MET11111790

610 Macek, W., Marciniak, Z., Branco, R., Rozumek, D., Królczyk, G.M., 2021. A fractographic study exploring the fracture surface topography of
611   S355J2 steel after pseudo-random bending-torsion fatigue tests. Measurement 178, 109443.
612   https://doi.org/10.1016/j.measurement.2021.109443

613 Malekipour, K., Mashayekhi, M., Badrossamay, M., 2021. Meso-scale damage mechanics modeling for high cycle fatigue behavior of additively
614   manufactured components. Mechanics of Materials 160, 103951. https://doi.org/10.1016/J.MECHMAT.2021.103951

615 Masoudi Nejad, R., Sina, N., Ghahremani Moghadam, D., Branco, R., Macek, W., Berto, F., 2022. Artificial neural network based fatigue life
616   assessment of friction stir welding AA2024-T351 aluminum alloy and multi-objective optimization of welding parameters. Int J Fatigue
617   160, 106840. https://doi.org/10.1016/J.IJFATIGUE.2022.106840

618 Meischel, M., Stanzl-Tschegg, S.E., Arcari, A., Iyyer, N., Phan, N., 2016. Influence of Corrosive NaCl solution on Life times of 7075 Aluminum
619   alloy under Combined Fatigue loading in the VHCF Regime. Procedia Structural Integrity 2, 1077–1084.
620   https://doi.org/10.1016/J.PROSTR.2016.06.138

621 Merson, E., Danilov, V., Merson, D., Vinogradov, A., 2017. Confocal laser scanning microscopy: The technique for quantitative fractographic
622   analysis. Eng Fract Mech. https://doi.org/10.1016/j.engfracmech.2017.04.026

623 Molent, L., Spagnoli, A., Carpinteri, A., Jones, R., 2017. Using the lead crack concept and fractal geometry for fatigue lifing of metallic structural
624   components. Int J Fatigue 102, 214–220. https://doi.org/10.1016/J.IJFATIGUE.2017.04.001

625 Newton, L., Senin, N., Gomez, C., Danzl, R., Helmli, F., Blunt, L., Leach, R., 2019. Areal topography measurement of metal additive surfaces
626   using focus variation microscopy. Addit Manuf 25, 365–389. https://doi.org/10.1016/J.ADDMA.2018.11.013

627 Pejkowski, Ł., Skibicki, D., 2019. Stress-strain response and fatigue life of four metallic materials under asynchronous loadings: Experimental
628   observations. Int J Fatigue 128, 105202. https://doi.org/10.1016/J.IJFATIGUE.2019.105202

629 Pelegatti, M., Lanzutti, A., Salvati, E., Novak, J.S., de Bona, F., Benasciutti, D., 2021. Cyclic plasticity and low cycle fatigue of an aisi 316l
630   stainless steel: Experimental evaluation of material parameters for durability design. Materials 14. https://doi.org/10.3390/MA14133588

631 Podulka, Przemysław, 2021. The Effect of Surface Topography Feature Size Density and Distribution on the Results of a Data Processing and
632   Parameters Calculation with a Comparison of Regular Methods. Materials 2021, Vol. 14, Page 4077 14, 4077.
633   https://doi.org/10.3390/MA14154077

634 Podulka, P, 2021. Reduction of the end-effect in surface texture analysis. J Phys Conf Ser 1736, 012013. https://doi.org/10.1088/1742-
635   6596/1736/1/012013

636 Rozumek, D., Lewandowski, J., Lesiuk, G., Marciniak, Z., Correia, J.A., Macek, W., 2022. The energy approach to fatigue crack growth of S355
637   steel welded specimens subjected to bending. Theoretical and Applied Fracture Mechanics 121, 103470.
638   https://doi.org/10.1016/J.TAFMEC.2022.103470

639 Rozumek, D., Marciniak, Z., Lesiuk, G., Correia, J.A., de Jesus, A.M.P., 2018. Experimental and numerical investigation of mixed mode I + II
640   and I + III fatigue crack growth in S355J0 steel. Int J Fatigue 113, 160–170. https://doi.org/10.1016/J.IJFATIGUE.2018.04.005

641 Sampath, D., Akid, R., Morana, R., 2018. Estimation of crack initiation stress and local fracture toughness of Ni-alloys 945X (UNS N09946) and
642   718 (UNS N07718) under hydrogen environment via fracture surface topography analysis. Eng Fract Mech 191, 324–343.
643   https://doi.org/10.1016/j.engfracmech.2017.12.010

Santos, L.M.S., Ferreira, J.A.M., Jesus, J.S., Costa, J.M., Capela, C., 2016. Fatigue behaviour of selective laser melting steel components.
    Theoretical and Applied Fracture Mechanics 85, 9–15. https://doi.org/10.1016/j.tafmec.2016.08.011

Santus, C., Romanelli, L., Grossi, T., Neri, P., Romoli, L., Lutey, A.H.A., Pedranz, M., Benedetti, M., 2022. Torsional-loaded notched specimen
    fatigue strength prediction based on mode I and mode III critical distances and fracture surface investigations with a 3D optical profilometer.
    Int J Fatigue 161, 106913. https://doi.org/10.1016/J.IJFATIGUE.2022.106913

Senin, N., Thompson, A., Leach, R.K., 2017. Characterisation of the topography of metal additive surface features with different measurement
    technologies. Meas Sci Technol. https://doi.org/10.1088/1361-6501/aa7ce2

651 Stamoulis, G., Carrere, N., 2020. Linear elastic analysis of the loading rate dependency of the fracture properties of structural adhesives in the
652   mixed mode I+II plane. Eng Fract Mech 106840. https://doi.org/10.1016/J.ENGFRACMECH.2019.106840

653 Stanzl-Tschegg, S.E., 2017. Influence of material properties and testing frequency on VHCF and HCF lives of polycrystalline copper. Int J Fatigue
654   105, 86–96. https://doi.org/10.1016/J.IJFATIGUE.2017.08.014

655 Strzelecki, P., Wachowski, M., 2022. Effect of the stress concentration factor on the final fracture zone of aluminium AW 6063 T6 for rotating
656   bending specimens. Mater Today Commun 31, 103766. https://doi.org/10.1016/J.MTCOMM.2022.103766

657 Todhunter, L.D., Leach, R.K., Lawes, S.D.A., Blateyron, F., 2017a. Industrial survey of ISO surface texture parameters. CIRP J Manuf Sci Technol
658   19, 84–92. https://doi.org/10.1016/J.CIRPJ.2017.06.001

659 Todhunter, L.D., Leach, R.K., Lawes, S.D.A., Blateyron, F., 2017b. Industrial survey of ISO surface texture parameters. CIRP J Manuf Sci Technol
660   19, 84–92. https://doi.org/10.1016/J.CIRPJ.2017.06.001

661 Tomczyk, A., Seweryn, A., 2017. Fatigue life of EN AW-2024 alloy accounting for creep pre-deformation at elevated temperature. Int J Fatigue
662   103, 488–507. https://doi.org/10.1016/j.ijfatigue.2017.06.037

663 Tomków, J., Janeczek, A., Rogalski, G., Wolski, A., 2020. Underwater Local Cavity Welding of S460N Steel. Materials 2020, Vol. 13, Page 5535
664   13, 5535. https://doi.org/10.3390/MA13235535

665 Vojtek, T., Pokluda, J., Hohenwarter, A., Pippan, R., 2013. Three-dimensional morphology of fracture surfaces generated by modes II and III
666   fatigue loading in ferrite and austenite. Eng Fract Mech 108, 285–293. https://doi.org/10.1016/J.ENGFRACMECH.2013.02.022

667 Walczak, M., Szala, M., 2021. Effect of shot peening on the surface properties, corrosion and wear performance of 17-4PH steel produced by
668   DMLS additive manufacturing. Archives of Civil and Mechanical Engineering 21, 1–20. https://doi.org/10.1007/S43452-021-00306-
669   3/FIGURES/13

670 Wang, Z., Wu, W., Qian, G., Sun, L., Li, X., Correia, J.A.F.O., 2019. In-situ SEM investigation on fatigue behaviors of additive manufactured Al-
671   Si10-Mg alloy at elevated temperature. Eng Fract Mech 214, 149–163. https://doi.org/10.1016/J.ENGFRACMECH.2019.03.040

672 Westermann, I., Pedersen, K.O., Børvik, T., Hopperstad, O.S., 2016. Work-hardening and ductility of artificially aged AA6060 aluminium alloy.
673   Mechanics of Materials 97, 100–117. https://doi.org/10.1016/J.MECHMAT.2016.02.017

674 Wietecha-Reiman, I.J., Segall, A., Zhao, X., Palmer, T.A., 2022. Combining Fractal and Topological Analyses to Quantify Fracture Surfaces in
675   Additively Manufactured Ti-6Al-4V. Int J Fatigue 107232. https://doi.org/10.1016/J.IJFATIGUE.2022.107232

676 Yao, M., Wang, H., Zhao, Y., Sha, J., 2018. Tension-tension fatigue behaviours of notched freestanding pure Ti foils with different thicknesses.
677   Int J Fatigue 114, 65–73. https://doi.org/10.1016/J.IJFATIGUE.2018.05.009

678 Zhang, N., Guo, S., He, G., Jiang, B., Zhou, L., Chen, Y., Liu, Y., 2022. Failure analysis of the carburized 20MnCr5 gear in fatigue working
679   condition. Int J Fatigue 161, 106938. https://doi.org/10.1016/J.IJFATIGUE.2022.106938

680